AGU ADVANCING EARTH AND SPACE SCIENCES

Water Resources Research

RESEARCH ARTICLE
10.1029/2025WR042386

A Semi-Analytical Model for Predicting the Depth-Averaged Maximum Longitudinal Velocity in Fully Ice-Covered Confluences

Zhiwei Li[1,2], Haokun Feng[1], Carlo Gualtieri[3], Bin Sun[1,2], Gang Chen[4], and Feifei Wang[1,2]

[1]School of Water Conservancy and Transportation, Zhengzhou University, Zhengzhou, China, [2]Yellow River Laboratory, Zhengzhou University, Zhengzhou, China, [3]Department of Structures for Engineering and Architecture, University of Napoli Federico II, Napoli, Italy, [4]Yunnan Key Laboratory of Water Security, Yunnan Survey and Design Institute of Water Conservancy and Hydropower, Kunming, China

Key Points:

- A model predicts depth-averaged maximum velocity in ice-covered confluences
- Maximum velocity in ice-covered confluences was studied using simulations
- Peak velocity at the recirculation zone's widest serves as a proxy for peak velocity

Correspondence to:
G. Chen,
zxm_232000@163.com

Citation:
Li, Z., Feng, H., Gualtieri, C., Sun, B., Chen, G., & Wang, F. (2026). A Semi-analytical model for predicting the depth-averaged maximum longitudinal velocity in fully ice-covered confluences. *Water Resources Research*, *62*, e2025WR042386. https://doi.org/10.1029/2025WR042386

Received 23 SEP 2025
Accepted 22 JAN 2026

Author Contributions:
Conceptualization: Zhiwei Li, Haokun Feng
Data curation: Zhiwei Li, Haokun Feng
Formal analysis: Zhiwei Li, Haokun Feng
Funding acquisition: Zhiwei Li
Investigation: Haokun Feng
Methodology: Zhiwei Li, Haokun Feng
Project administration: Zhiwei Li, Gang Chen
Resources: Zhiwei Li, Gang Chen
Software: Zhiwei Li, Haokun Feng
Supervision: Zhiwei Li, Gang Chen
Validation: Haokun Feng
Visualization: Zhiwei Li
Writing – original draft: Haokun Feng
Writing – review & editing: Zhiwei Li, Carlo Gualtieri, Bin Sun, Gang Chen, Feifei Wang

Abstract At river confluences, the complex hydrodynamics result in significant alterations to flow structures, and the maximum velocity zone serves as one of the primary drivers of pollutant transport and riverbed erosion. This study investigates maximum longitudinal velocity formation in fully ice-covered confluences, statistically validating the substitution of depth-averaged maximum longitudinal velocity at the widest recirculation section for depth-averaged maximum longitudinal velocity. In this study, a semi-analytical model is developed to address transitional shear layer modes: (a) wake mode employing dual control volumes, and (b) mixing layer mode treating converging flow as a single control volume. The momentum equation incorporating secondary flow effects predicts maximum depth-averaged velocities, verified against 3D simulations and experimental data with mean errors below 0.42%. Results confirm both models accurately predict velocities within their respective flow regimes, providing the first mechanistic framework for ice-covered confluence hydrodynamics.

1. Introduction

River confluences, which represent fundamental geomorphic units within river networks, are widely distributed in natural rivers. These channels often exhibit intricate hydrodynamic behaviors (Bradbrook et al., 2000; Constantinescu & Gualtieri, 2024; Gualtieri et al., 2020; Leite Ribeiro et al., 2012b; Lewis et al., 2020; Weber et al., 2001; Yuan, Zhu, et al., 2022, Yuan, Qiu et al., 2023), which significantly influence bed morphology (Constantinescu et al., 2014, 2016), sediment (Cheng & Constantinescu, 2018; Leite Ribeiro et al., 2012a; Szupiany et al., 2012; Umar et al., 2018; Yuan et al., 2018), contaminant transport (Tang et al., 2018; Zhang et al., 2023), and thermal mixing (Bahmanpouri et al., 2022; Rhoads & Johnson, 2018).

Best (1987) classified the flow zones within confluence channels into six categories: stagnation zone, deflection zone, separation zone, maximum velocity zone, recovery zone, and shear layer zone. These flow characteristics significantly influence key environmental factors such as temperature, sediment suspension, nutrient dynamics, and oxygen concentration within the confluence channel, thereby shaping the local ecosystem (Qiu et al., 2025; Yuan, Xu, et al., 2022; Zheng et al., 2020). Due to their unique hydrodynamic and nutrient distribution characteristics, confluence zones are vital habitats and feeding grounds for fish and aquatic organisms (Liao et al., 2003; Prechtel et al., 2018; Zhang et al., 2015), Additionally, multiple hypotheses concerning geomorphic dynamics at confluence zones have been advanced, including the effects of maximum velocity zones, intense turbulence, shear layers, and separation zones (Guillén-Ludeña et al., 2015, 2016; Rhoads et al., 2009; Rhoads & Sukhodolov, 2001; Rice et al., 2006; Weber et al., 2001).

The formation of the maximum velocity zone results from streamline contraction induced by the low-velocity separation zone (Best, 1987; Shakibainia et al., 2010). This zone is situated near the point where the separation zone reaches its maximum width, commonly referred to as the vena contracta (Shakibainia et al., 2010). Identifying the location and magnitude of the maximum velocity is critical, given that shear stress and scour typically peak in this region. Furthermore, the maximum velocity zone notably affects pollutant dynamics and adsorption processes (Ashmore, 1982; Ashmore et al., 1992). Additionally, the maximum velocity affects pollutant transport and adsorption (Liu et al., 2021; Yang et al., 2009; Yu et al., 2020). The formation mechanisms and characteristics of the maximum velocity zone have been investigated through field and flume experiments,

with numerical models also serving as critical tools for analyzing confluence flow dynamics. These models include one-dimensional (Rice et al., 2006), two-dimensional (Holzner et al., 2024; Yan et al., 2022), and three-dimensional (Behzad et al., 2024; Bradbrook et al., 1998, 2000; Lazzarin et al., 2026; Sandilya et al., 2025) approaches.

Rivers in cold regions are influenced by low winter temperatures, which result in ice cover formation on the water surface. Compared to open channels, the ice cover's underside and riverbed introduce unique roughness differences, leading to asymmetric flow within confluence channels (Zhong et al., 2018). Ice-covered confluence channels exhibit distinct hydrodynamic and geomorphic traits compared to open channels (Lau & Krishnappan, 1981; Morse & Hicks, 2005; Robert & Tran, 2012; Zare et al., 2016). Biron et al. (2019) examined 3D flow differences at confluences under ice-covered and open conditions based on field experiments and proposed a conceptual model to describe the mixing layer structure. Therefore, exploring confluence dynamics under ice-covered conditions is essential. While many studies have extensively examined separation zones at open-channel confluences, the characteristics of the maximum velocity zone under ice-covered conditions remain to be explored.

Ice-covered channels exhibit distinct hydrodynamic characteristics compared to open channels, with the ice cover introducing additional challenges for channel management (Ettema, 2002). Although numerical simulations can determine the maximum longitudinal velocity, these complex models require extensive empirical parameters (e.g., turbulence closure, roughness specification) and entail high computational costs, making them less suitable for rapid assessment or numerous scenario analyses. Furthermore, direct measurement of the maximum velocity in ice-covered rivers using Acoustic Doppler Current Profilers (ADCPs) is particularly difficult and hazardous. During floods or other extreme events, timely and rapid estimation of the maximum velocity is often required for operational decisions (e.g., ice jam flood forecasting, infrastructure safety assessment), yet direct measurement under such conditions is often infeasible or impractical (Kakavandi et al., 2024), while numerical modeling for each scenario is time-consuming. Consequently, this study also develops a computationally efficient semi-analytical alternative method for predicting the maximum depth-averaged longitudinal velocity in ice-covered confluence channels, based on an understanding of the key physical mechanisms governing the flow. Therefore, this study proposes a computationally efficient alternative approach for predicting the depth-averaged maximum longitudinal velocity in ice-covered confluence channels. The remainder of this paper is structured as follows. Sections 2 and 3 outline the experimental flume setup and three-dimensional numerical simulations, respectively. Section 4 investigates the dynamic characteristics of flow velocity under ice-covered conditions. Based on experimental and simulation results, Section 5 proposes equations for calculating the depth-averaged maximum longitudinal velocity. The accuracy of the equation is evaluated in Section 6, while Section 7 discusses the secondary flow coefficient incorporated in the equations and addresses the model's limitations.

2. Experimental Setup and Instrumentation

This experiment was conducted in a recirculating flume at Zhengzhou University, China, capable of varying junction angles θ and discharge ratios η. Ten experimental conditions were designed, incorporating two junction angles (60° and 90°) and five discharge ratios ranging from 0.15 to 0.43. These values were selected considering previous studies in natural confluences (0.15–0.43) (Boyer et al., 2006; Rhoads & Sukhodolov, 2008). Furthermore, the Froude number (0.19–0.22) is consistent with previous field (0.03–0.85) and laboratory studies (0.02–0.5) (Yu et al., 2020). Details of the experimental configuration are provided in Table 1.

The main channel of the flume is 14 m long and 1 m wide, while the tributary channel measures 3 m in length and 0.5 m in width. The downstream section of the flume is connected to a bottom water tank, enabling water recirculation through transport pipes linking the upstream sections of the main and tributary channels to the water tank. The flume walls were made of glass, and the longitudinal slope was set at $S_0 = 0.01\%$. The discharge ratios in the main and tributary channels were adjusted by controlling the pump power along the transport pipes and monitored using electromagnetic flowmeters (accuracy: 3 cm^3/s) installed on each pipe. The water depth in the flume was controlled by adjusting the tailgate opening located at the downstream end of the main channel and was set at 0.25 m using the depth-measuring probe (accuracy: 0.1 mm) for monitoring.

To ensure a fully developed flow upstream of the confluence, honeycomb-patterned short tubes were installed at the upstream sections of the main and tributary channels. Given the analogous hydraulic-relevant characteristics (continuous, rigid, impermeable, buoyant) of rigid foam board (Expanded Polystyrene, EPS) and ice cover, EPS

Table 1
Experiment Cases Under Different Discharge Ratios

Case	A1	A2	A3	A4	A5	B1	B2	B3	B4	B5
θ (°)	60	60	60	60	60	90	90	90	90	90
Q_m (m^3/s)	0.0675	0.0625	0.06125	0.05	0.05	0.0675	0.0625	0.06125	0.05	0.05
u_m (m/s)	0.27	0.25	0.245	0.2	0.2	0.27	0.25	0.245	0.2	0.2
R_m	39,500	41,501	35,850	33,201	33,201	39,500	41,501	35,850	33,201	33,201
Q_t (m^3/s)	0.0117	0.0156	0.024	0.025	0.0375	0.0117	0.0156	0.024	0.025	0.0375
u_t (m/s)	0.093	0.125	0.19	0.2	0.3	0.093	0.125	0.19	0.2	0.3
R_t	10,270	15,563	21,040	24,900	37,350	10,270	15,563	21,040	24,900	37,350
F_{pc}	0.2	0.2	0.22	0.19	0.22	0.2	0.2	0.22	0.19	0.22
R_{pc}	46,340	51,860	49,900	49,801	58,102	46,340	51,860	49,900	49,801	58,102
M_r	0.06	0.12	0.30	0.5	1.13	0.06	0.12	0.30	0.5	1.13
η	0.15	0.2	0.28	0.33	0.43	0.15	0.2	0.28	0.33	0.43

Note. Q is the discharge; F and R are the Froude number and the Reynolds number after the quasi-equilibrium stage; M_r is the momentum ratio calculated by $(Q_t u_t)/(Q_m u_m)$. The subscripts "m", "t" and "pc" represent the main channel, the tributary and the post-confluence, respectively; η is the discharge ratio calculated by $Q_t/(Q_t + Q_m)$.

foam boards were applied to simulate the latter (Sui et al., 2010; Wang et al., 2020, 2021), with dimensions of 5.5 m × 1 m in the main channel and 2 m × 0.5 m in the tributary channel. Existing research indicates that Manning's roughness coefficient n for EPS is approximately 0.0105, slightly higher than that of the flume bed (Li et al., 2024). Based on those studies (Wang et al., 2020, 2021), which successfully elucidated key hydraulic properties under the ice cover, the EPS foam board was deemed a suitable material for this study's objectives. During the test, the fixed simulated ice cover was tightly attached to the water surface and could not fluctuate with the flow, but could float up and down with the change of water depth. The experimental setup, with a junction angle of 90°, is illustrated in Figure 1.

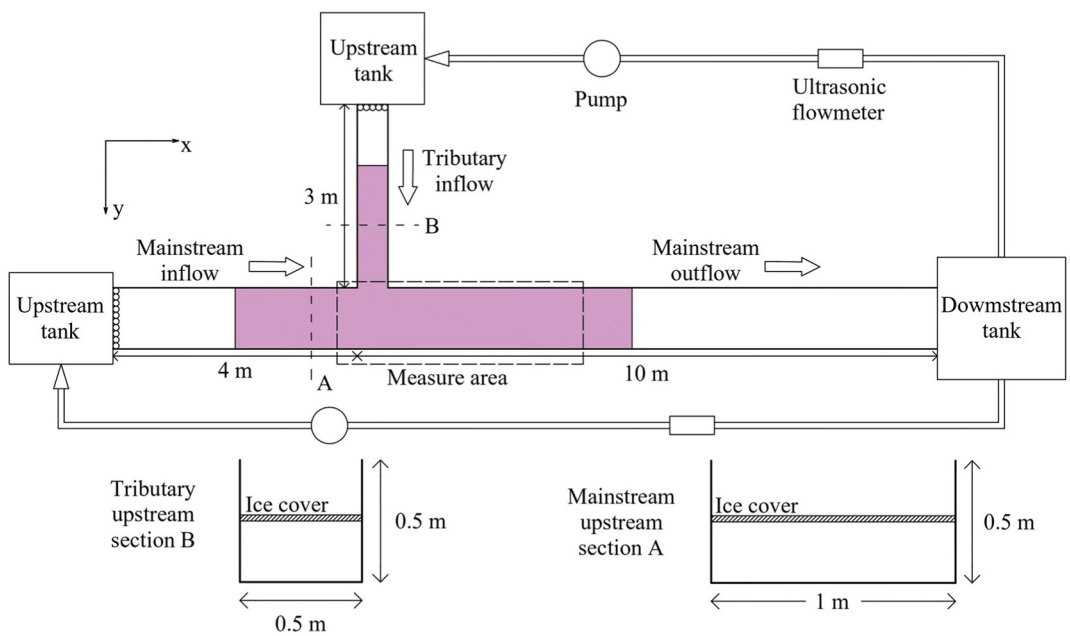

Figure 1. Sketch of the full-coverage ice cover configuration under a 90° junction angle; the pink-shaded regions delineate the spatial extent of ice cover.

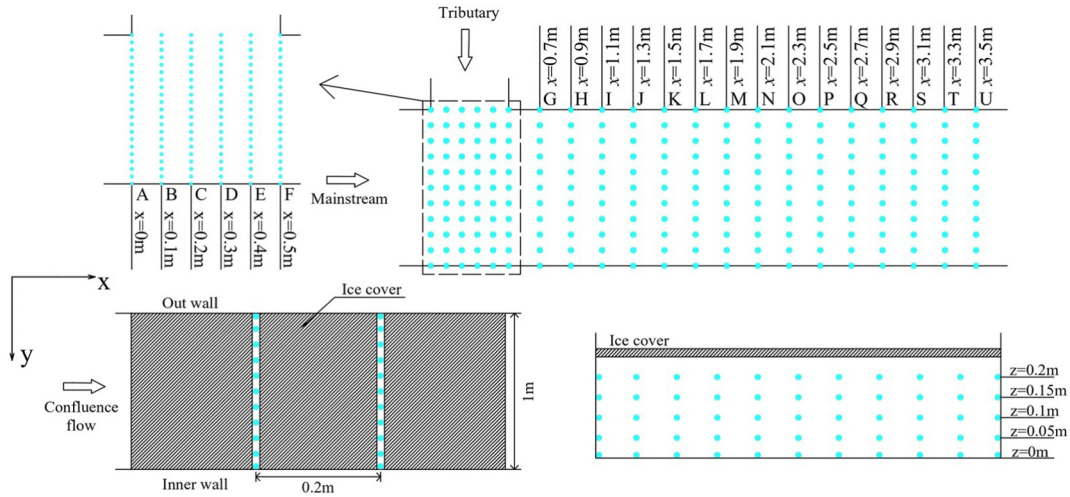

Figure 2. Schematic top view and cross-section of the measuring point arrangement, taking the 90° junction angle case for example.

To guarantee that the first measurement section was fully influenced by the ice cover and that the flow was adequately developed, it was positioned 2 m downstream from the beginning of the ice-covered confluence. A total of 20 measurement sections were established, with the first five sections spaced at 10 cm and the remaining 15 at 20 cm intervals. Each measurement section included 11 vertical measurement lines spaced at 10 cm apart, and each line contained five measurement points spaced at 5 cm intervals. The distribution of measurement sections and points is shown in Figure 2.

The three-dimensional velocity field of the flow was measured using a SonTek 3D acoustic Doppler velocimeter (ADV) (accuracy: 0.01 cm/s). This device operates based on the Doppler effect, assuming that the particle velocity within the sampling volume equals the flow velocity. The sampling volume is located 5 cm in front of the probe and has a volume of 0.42 cm^3. The ADV was sampled continuously at 100 Hz for 60 s. To ensure accurate velocity measurements, only data with a correlation coefficient greater than 85% and a signal-to-noise ratio (SNR) above 15 were retained. Talcum powder was added to the water throughout the entire experiment to enhance the acoustic signal. The ADV was fixed on a movable frame, and the position of the frame was manually adjusted and calibrated using a steel ruler (accuracy: 0.1 cm).

3. Numerical Model

3.1. Turbulence Model and Domain Meshes

The flow field within the confluence flume was derived by solving the 3D model of the Reynolds-Averaged Navier-Stokes (RANS) equations. The continuity and momentum equations for incompressible fluid under the Boussinesq approximation in the Cartesian coordinate system are expressed as follows (Marzouk & Huckaby, 2009):

$$\frac{\partial \rho u_i}{\partial x_i} = 0 \tag{1}$$

$$\frac{\partial \rho u_i}{\partial t} + \frac{\partial \rho u_j u_i}{\partial x_j} = -\frac{\partial p}{\partial x_i} + \frac{\partial}{\partial x_j}\left(\rho(\nu + \nu_t)\left(\frac{\partial u_i}{\partial x_i} + \frac{\partial u_j}{\partial x_i}\right)\right) \tag{2}$$

$$\nu_t = C_\mu \frac{k^2}{\varepsilon} \tag{3}$$

where t is time, s; u_i is the flow velocity of each direction, m/s; p is the pressure, pa; ρ is the fluid density, kg/m^3; ν is the molecular kinematic coefficient, m^2/s; ν_t is the eddy viscosity coefficient, m^2/s; C_μ is an empirical constant,

which was calculated as 0.085; k is the turbulence kinetic energy, m^2/s^2; ε is the turbulence dissipation rate. The RNG k–ε model was selected based on its demonstrated efficacy in simulating confluence hydrodynamics through quantitative validation studies. According to Shen et al. (2022), a systematic comparison of the Reynolds Stress Model (RSM), standard k–ε model, and RNG k–ε model revealed that the RNG k–ε model outperformed others in capturing complex flow structures at confluences. This advantage arises because the RNG k–ε model incorporates a modified formulation for turbulent viscosity and accounts for rotational and swirling effects, enabling more accurate prediction of flows with high strain rates and significant streamline curvature—a critical feature in confluence zones. Consequently, compared to other turbulence models (Bradbrook et al., 2000; Mahmodinia & Javan, 2021; Shen et al., 2019, 2023; Shi et al., 2025), the RNG k–ε model is more accurate for confluences. Using the RNG k-ε turbulence model, the turbulent kinetic energy k and dissipation rate ε are computed using the following expressions (Yakhot & Orszag, 1986):

$$\frac{\partial k}{\partial t} + u_j \frac{\partial k}{\partial x_j} = -u_i' u_j' \frac{\partial u_i}{\partial x_j} + \frac{\partial u}{\partial x_j}\left(\frac{K_m \partial k}{\sigma_k \partial x_j}\right) - \varepsilon \tag{4}$$

$$\frac{\partial \varepsilon}{\partial t} + u_j \frac{\partial \varepsilon}{\partial x_j} = -C_{\varepsilon 1} \frac{\varepsilon}{k} u_i' u_j' \frac{\partial u_i}{\partial x_j} + \frac{\partial}{\partial x_j}\left(\frac{K_m \partial \varepsilon}{\sigma_\varepsilon \partial x_j}\right) - C_{\varepsilon 2} \frac{\varepsilon}{k} - R \tag{5}$$

$$K_m = \nu\left(1 + \left(\frac{\nu_t}{\nu}\right)^{1/2}\right)^2 \tag{6}$$

$$R = \frac{C_\mu \eta'^3 \left(1 - \eta'/\eta_0'\right)\varepsilon^2}{\left(1 + \beta' \eta'^3\right) k} \tag{7}$$

$$\eta_0' = \frac{k}{\varepsilon}\left[\left(\frac{\partial u_i}{\partial x_j} + \frac{\partial u_j}{\partial u_i}\right)\frac{\partial u_i}{\partial x_j}\right]^{1/2} \tag{8}$$

where K_m is the time-averaged strain rate; R is the extra strain rate; η' is the dimensionless shear rate, η_0' is the fixed point value $\eta_0' = 4.38$; $C_{\varepsilon 1}$ and $C_{\varepsilon 2}$ are constants that are usually determined from benchmark experiments and have values of 1.42 and 1.68, $C_{\varepsilon 2}$ is the power law of turbulence decay, σ_k and σ_ε are the reciprocals of the effective turbulent Prandtl number of k and ε, respectively, and both are 0.7179; β' is an empirical constant, and its value is 0.012 (Shen et al., 2019, 2021).

The finite volume method for solving the coupled unsteady governing equations was established using the PimpleFoam solver in the OpenFOAM software. The PimpleFoam solver incorporates the PIMPLE algorithm, which combines the SIMPLE and PISO algorithms. The PIMPLE algorithm solves transient incompressible flow over long-time steps efficiently. The smoothSolver algorithm was applied to compute the implicit matrices for velocity, turbulent kinetic energy, and turbulent dissipation rate variables. OpenFOAM's nutkRoughWall-Function, which directly specifies the roughness height (k_s) and roughness constant (C_s). k_s was calibrated to 0.005 m for the bed and sidewall boundaries, and to 0.009 m for the ice cover. A uniform $C_s = 0.5$ was maintained across all surfaces. These parameter settings align with the experimental conditions. Parallel computing was employed to save computational time. The time step was adjusted based on the Courant number, which was maintained below 1 in all cases. The detailed configuration of the OpenFOAM solver is presented in Table 2.

The boundary and initial conditions in the numerical simulation were determined based on experimental conditions. The main and tributary inflows were set with fixed flow rates, while the outlet was set with a zero-pressure gradient. The ice cover and wall boundaries were set as no-slip walls. An unstructured rectangular mesh was employed for the simulation. To accurately capture flow separation phenomena, local mesh refinement was implemented with increased vertical resolution near the walls and enhanced grid density in the confluence region, as explicitly visualized in Figure 3. The maximum mesh size in the flume was set to $10 \times 10 \times 10$ mm, while the minimum mesh size near the walls was $1.3 \times 1.3 \times 1.3$ mm, as present in Figure 3. The near-wall grid resolution ($1.3 \times 10 \times 10$ mm) was governed by y^+ criteria ($y^+ = 20$) in the numerical framework. The computational domain comprised 4,906,535 unstructured grids. Grid Convergence Index (GCI) analysis yielded a value of 2.3%

Table 2
Summary Table of Numerical Simulation Settings

Category	Parameter	Setting/Method
Solver and Algorithm	Solver	PimpleFoam
	Algorithm	PIMPLE and smoothSolver
	Time step	Adaptive (based on Courant number)
	Max Courant Number	Below 1
Boundary condition	Inlet	Velocity
	Outlet	zoreGradient
	Wall	noSlip
	Ice-cover	noSlip
Turbulence model	Model	RNG k-ε model
	Wall function	epsilonWallFunction
Discretization Schemes	Time derivatives	Euler
	Laplacian term	Gauss linear
	Gradient term	Gauss linear
	Convection Term	Gauss upwind and Gauss linear
	Mesh type	Unstructured hexahedral
Mesh	Maximum mesh	10 × 10 × 10 mm
	Minimum mesh	1.3 × 1.3 × 1.3 mm
	Total number	4,906,535

(Celik et al., 2008), confirming solution independence from grid size. Complete grid sensitivity studies are documented in Appendix A.

The wall function was applied at the wall boundaries using the following equation:

$$U^* = \begin{cases} y^* & y^* < 11.63, \\ \frac{1}{\kappa}\ln(Ey^*) & y^* \geqslant 11.63, \end{cases} \tag{9}$$

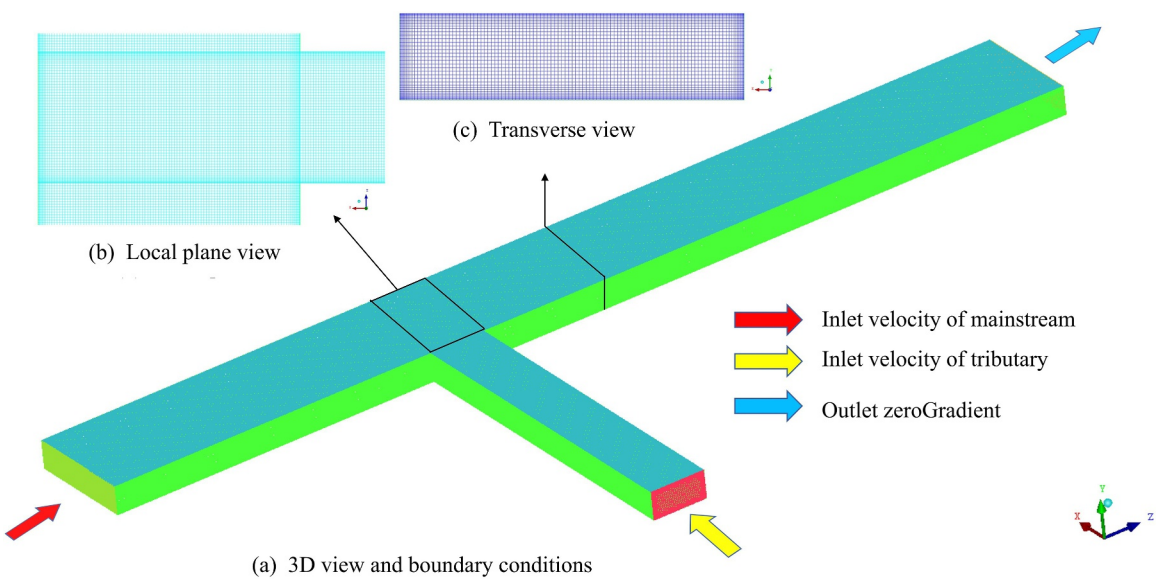

Figure 3. Computational domain, boundary conditions, and mesh details. (a) Boundary conditions and the computational domain. (b) Mesh refinement in the confluence zone, highlighting enhanced resolution near sidewalls and the confluence corner. (c) Cross-sectional mesh demonstrating vertical refinement near the bed and walls.

Table 3
Key Residual Criteria and Results of the Velocity of the Numerical Models

Statistical indicators	Formula	Range	Ideal value	Velocity	
				90°	60°
Bias (m/s)	$\frac{1}{n}\sum_{i=1}^{n}(u_{i,\mathrm{sim}} - u_{i,\mathrm{ex}})$	$(-\infty,+\infty)$	0	0.0042	0.0297
Relative bias	$\frac{1}{n}\sum_{i=1}^{n}(u_{i,\mathrm{sim}} - u_{i,\mathrm{ex}})/u_{i,\mathrm{ex}}$	$(-1,1)$	0	0.0157	0.0841
MSE (m/s)	$\frac{1}{n}\sum_{i=1}^{n}(u_{i,\mathrm{sim}} - u_{i,\mathrm{ex}})^2$	$(0,+\infty)$	0	0.0018	0.0021
RMSE (m/s)	$\sqrt{\frac{1}{n}\sum_{i=1}^{n}(u_{i,\mathrm{sim}} - u_{i,\mathrm{ex}})^2}$	$(0,+\infty)$	0	0.0426	0.0455
MAE (m/s)	$\frac{1}{n}\sum_{i=1}^{n}\lvert u_{i,\mathrm{sim}} - u_{i,\mathrm{ex}}\rvert$	$(0,+\infty)$	0	0.0322	0.0366
AME (m/s)	$\max\lvert u_{i,\mathrm{sim}} - u_{i,\mathrm{ex}}\rvert$	$(0,+\infty)$	0	0.1555	0.1311

Note. $u_{i,ex}$ represents the experimental velocity data and $u_{i,sim}$ denotes the corresponding simulated velocity.

$$U^* = \frac{\mu_0 C_u^{1/4} k^{1/2}}{\tau_w/\rho} \tag{10}$$

$$y^* = \frac{\rho \mu_0 C_u^{1/4} k^{1/2} y}{u} \tag{11}$$

where U^* and y^* are both dimensionless parameters and represent velocity and distance; κ is the Karman constant and the value is 0.41; E is the experiment constant and the value is 9.81; y is the distance between the node and the wall, m; τ_w is the wall shear stress; k is the turbulent kinetic energy at the calculation node; and μ_0 is the fluid dynamic viscosity.

3.2. Validation of the Numerical Simulations

The solvers available in the open-source OpenFOAM software have been widely used in numerous studies (Fuentes-Pérez et al., 2018; Shaheed et al., 2019). In this section, the numerical model data are compared with experimental data to provide a clearer assessment of the model's performance. The evaluation follows the criteria introduced by Bennett et al. (2013), which include key residual metrics such as bias, relative bias, mean squared error (MSE), root mean squared error (RMSE), mean absolute error (MAE), and absolute maximum error (AME). The results are shown in Table 3, and Figure 4 compares simulated and experimental longitudinal velocities at the J section under Cases A5 and B5, demonstrating transverse distributions (a–f) and vertical distributions (g–i) of the flow field. The longitudinal flow velocity u is expressed as a dimensionless number u/u_d, where u_d is the cross-sectional average flow velocity in the post-confluence channel being $u_d = (Q_t + Q_m)/W_d h$, and W_d is the width of the main channel, h is the water depth. Figure 4 (g, j, k) exhibits diminished longitudinal velocities at mid-depth, resulting from the maximum width of the recirculation zone occurring near intermediate depths. Lower longitudinal velocities along the recirculation boundaries generate transverse shear stresses. Consequently, flow at mid-depth experiences greater transverse shear forces than near the ice cover and bed, producing the observed velocity dip.

It was found that the average error across different cases generally remained within 10%, with the maximum error near the recirculation zone boundary, bed and wall surfaces. This discrepancy may originate from the selected y^+ value of 20 in the numerical simulation, which requires the use of a wall-function approach. This method simplifies boundary layer resolution by neglecting the viscous sublayer and buffer layer, but may compromise accuracy in regions with strong flow separation, such as near separation or recirculation zones. Although the model has inherent limitations in resolving complex separated flows, its accuracy in capturing the flow characteristics of interest—primarily including the size of separation/recirculation zones and depth-averaged maximum longitudinal velocity—remains reasonable for engineering applications (Shakibainia et al., 2010; Shen et al., 2022). If data points near the wall and the recirculation zone boundary are excluded, the average error was less than 5%, demonstrating the accuracy of the numerical simulations.

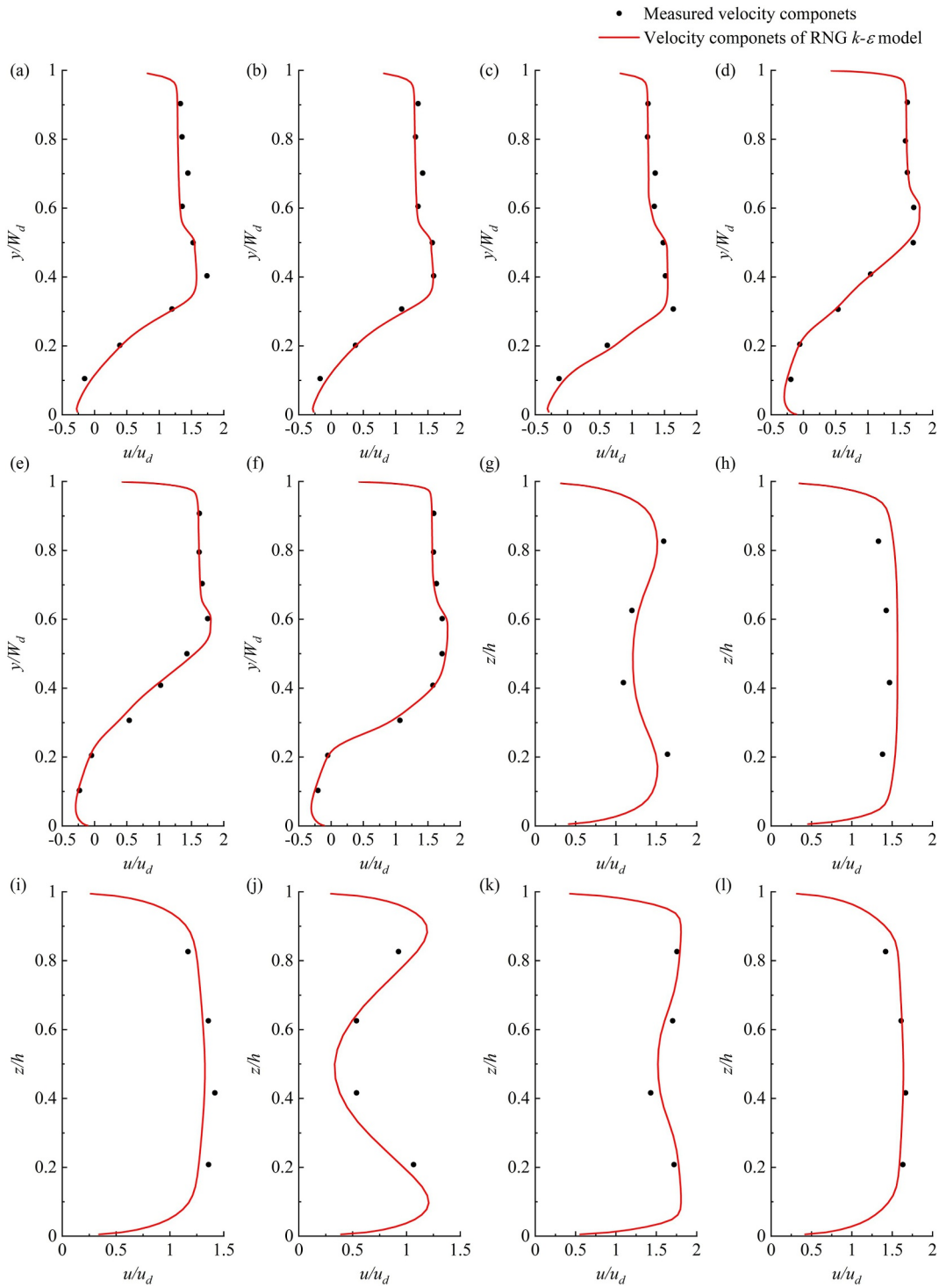

Figure 4. Comparison between numerical results and experimental data for the lateral (a)–(f) and vertical (g–l) distribution of the dimensionless longitudinal velocity at (j) Subfigures include (a) $z = 0.15$ m, (b) $z = 0.1$ m, (c) $z = 0.05$ m, (g) $y = 0.3$ m, (h) $y = 0.5$ m, (i) $y = 0.7$ m for Case A5, and (d) $z = 0.15$ m, (e) $z = 0.1$ m, (f) $z = 0.05$ m, (g) $y = 0.3$ m, (h) $y = 0.5$ m, (i) $y = 0.7$ m for Case B5.

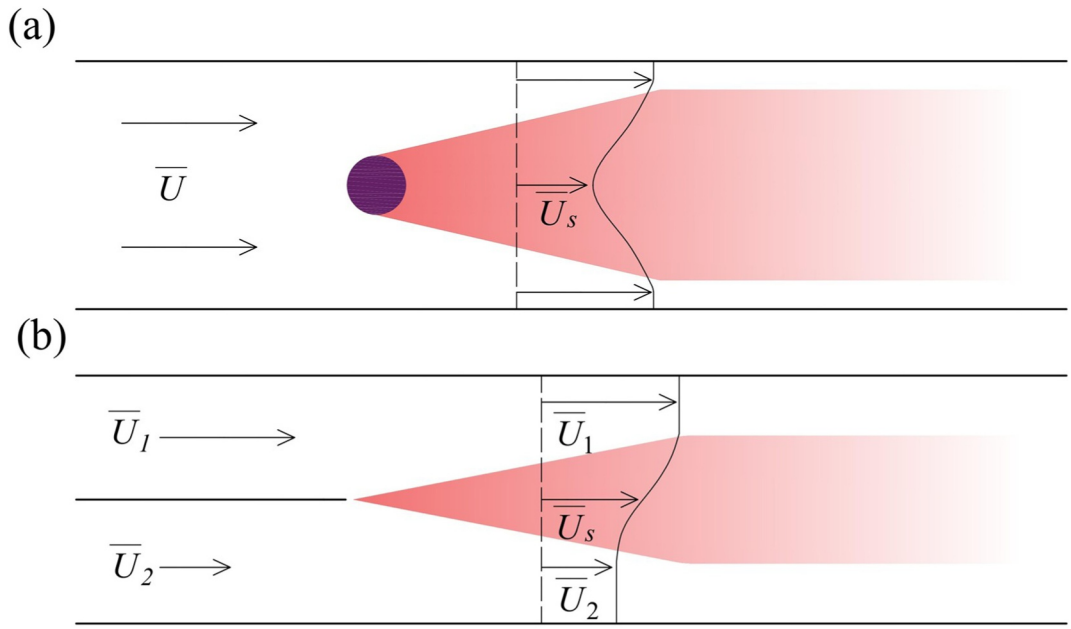

Figure 5. Type of shear layer: (a) wake and (b) mixing-layer (adapted from Rhoads & Sukhodolov, 2008).

4. Longitudinal Velocity Distribution

4.1. The Impact of the Shear Layer on Longitudinal Flow Velocity

Velocity differentials between the main channel and tributary generate a shear layer comprising quasi-two-dimensional vortices with near-vertical axes. Confluence mixing follows two distinct regimes: wake mode and mixing-layer mode (Sukhodolov et al., 2023), as illustrated in Figure 5. During its formation, the shear layer exhibits the wake mode and evolves to the mixing-layer mode as it progresses downstream.

In the wake mode, the mean velocity within the shear layer is lower than adjacent flows, featuring significant transverse velocity gradients (Rhoads & Sukhodolov, 2008) and elevated Reynolds shear stresses $<u'v'>$ compared to external regions (Yuan et al., 2016). This produces dual velocity peaks flanking the shear layer within the contracted flow section, as shown in Figures 5a and 6 (Rhoads & Sukhodolov, 2001; Shakibainia et al., 2010). Consequently, the shear layer partitions the flow into two control volumes: V_1 (mainstream inflow) and V_2 (tributary inflow). The hypothetical interface between these volumes is defined by loci of minimum velocity within the shear layer at each cross-section. For V_1, bounded by the hypothetical interface and outerwall, maximum velocities arise under the combined influence of both the shear stress from the wall and shear layer. Similarly, V_2—constrained between the recirculation zone boundary and hypothetical interface—develops peak velocities modulated by the shear stress from the recirculation zone and shear layer. Figure 7a schematizes V_1 and V_2, and their associated shear stress distributions.

The position of the shear layer is predominantly governed by the momentum ratio (Boyer et al., 2006; De Serres et al., 1999; Jiang et al., 2023), thereby yielding an expression for the hypothetical interface location as follows:

$$\frac{W_2}{W_1} = \frac{Q_{\mathrm{TUS}} \cdot \sin(\theta')}{Q_{\mathrm{TUS}} \cdot \cos(\theta') + Q_{\mathrm{MUS}}} + \varphi \tag{12}$$

where φ is an empirical coefficient delineating the impact of secondary flows on the hypothetical interface's position, calibrated as 0.04 through simulated results; W_1 and W_2 are the effective cross-sectional widths of the flow for V_1 and V_2, respectively; θ' is the inflow angle of the tributary flow. When the shear layer transitions into the mixing-layer mode, as shown in Figure 5b and a single velocity peak appears along the horizontal measurement line, accompanied by a velocity gradient within the shear layer from the high-velocity control volume toward the low-velocity control volume. At the entrance to the contracted section, the shear layer in wake mode

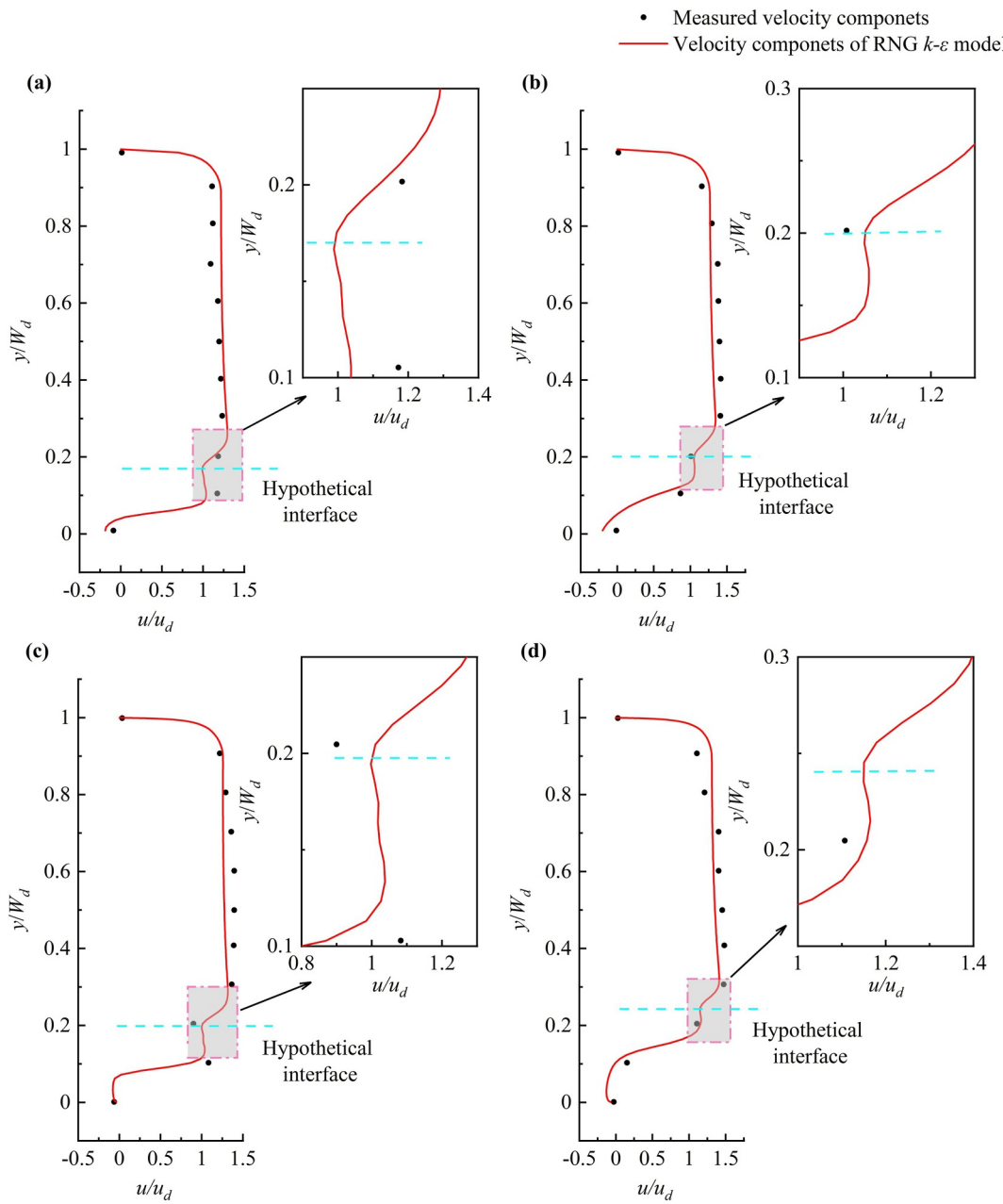

Figure 6. Transverse distributions of longitudinal velocity in wake mode shear layer: Case A1 at (a) $x = 0.7$ m, $z = 0.125$ m and (b) $x = 1.1$ m, $z = 0.125$ m; Case B1 at (c) $x = 0.7$ m, $z = 0.125$ m and (d) $x = 0.9$ m, $z = 0.125$ m.

divides the flow into two parts, as illustrated in Figure 8. As the flow develops downstream, the wake mode evolves into the mixing-layer mode, and the contraction section is analyzed using a single control volume, V_3, whose schematic is shown in Figure 7b. This control volume is subjected to shear stresses from both the wall and the recirculation zone, leading to the formation of a single velocity peak within V_3, as depicted in Figure 7.

4.2. The Impact of the Ice Cover and Recirculation Zone on Longitudinal Flow Velocity

In ice-covered channels, open-channel flow transitions to a confined conduit while retaining essential open-channel flow characteristics (Zhang et al., 2021). The ice cover is treated as a no-slip boundary that imposes additional shear stresses on the contracting flow, fundamentally altering the vertical distribution of longitudinal velocity (Tsai & Ettema, 1994), as shown in Figure 9. Consequently, the maximum longitudinal velocity shifts

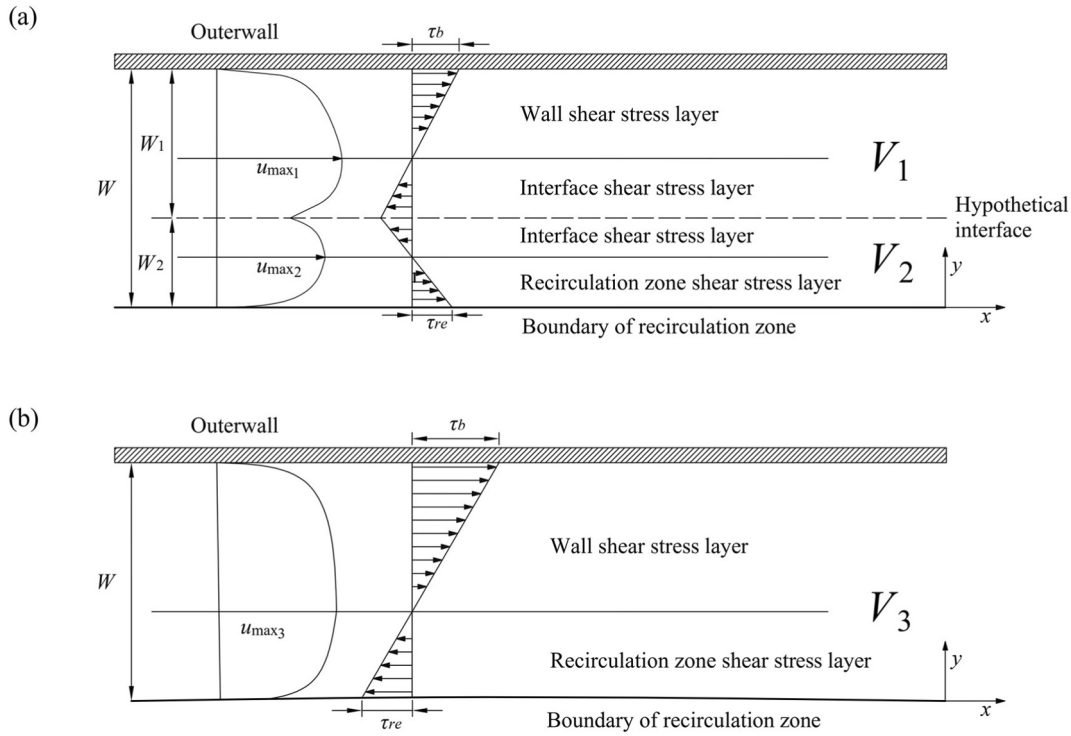

Figure 7. Sketch of control volume, (a) the shear layer in the wake mode; (b) the shear layer in the mixing-layer mode, τ_w is the wall shear stress, τ_{re} is the shear stress from the recirculation zone, and W is the effective flow section.

from near the free surface to the inner water. The presence of the ice cover causes an increase in the wetted perimeter, elevates flow resistance, and reduces discharge capacity (Peters et al., 2017). Owing to the differential roughness between the ice cover and channel bed, the velocity profile exhibits vertical asymmetry. Most studies employ Einstein's resistance separation theory (Einstein, 1942), which segments the flow at the maximum longitudinal flow velocity locus into two hydraulically independent layers: the upper ice layer and lower bed layer. Each layer follows a distinct two-power law distribution, influenced exclusively by ice-cover roughness (k_i) and bed roughness (k_b), respectively. The shear stress τ_{zx} varies linearly with depth, reaching maxima at the ice cover underside (τ_i) and channel bed (τ_b) (Tsai & Ettema, 1994). Thus, the Reynolds shear stress is expressed as:

$$\tau_{zx} = \tau_b - (\tau_b + \tau_i)\frac{z}{H} \tag{13}$$

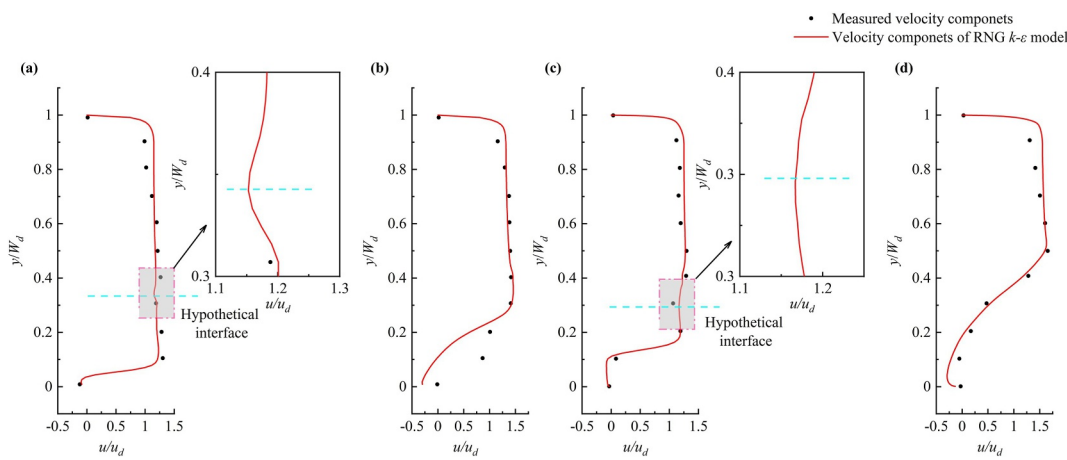

Figure 8. Transverse distributions of longitudinal velocity in mixing-layer mode for the shear layer: Case A4 at (a) $x = 0.7$ m, $z = 0.125$ m and (b) $x = 1.3$ m, $z = 0.125$ m; Case B4 at (c) $x = 0.7$ m, $z = 0.125$ m and (d) $x = 1.3$ m, $z = 0.125$ m.

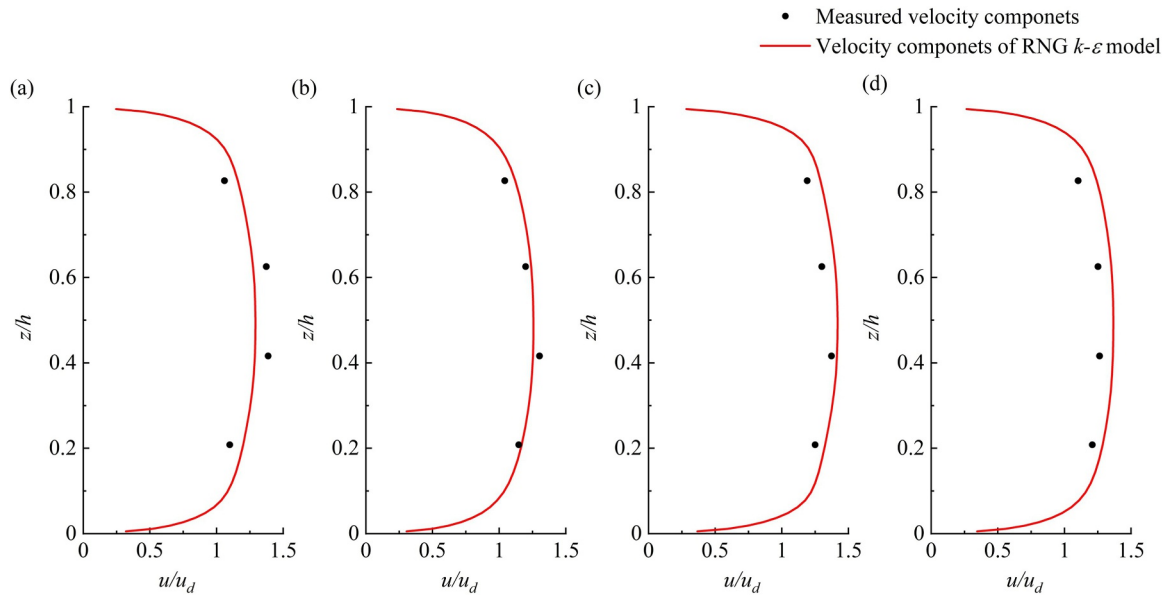

Figure 9. Vertical distribution of longitudinal velocity; Case A2 at (a) $x = 0.9$ m, $y = 0.5$ m, (b) $x = 0.9$ m, $y = 0.8$ m; Case B2 at (c) $x = 0.9$ m, $y = 0.5$ m, (d) $x = 0.9$ m, $y = 0.8$ m.

In rectangular channels, the maximum longitudinal velocity typically occurs at the position of zero shear stress ($\tau_{zx} = 0$). However, within contracted flow sections, a deviation arises between the locations of maximum longitudinal velocity and zero shear stress due to the presence of three-dimensional recirculation zones. When a tributary enters the main channel at an oblique angle, its transverse momentum deflects the main flow toward the outer wall. Concurrently, acute junction angles induce flow separation downstream, forming a recirculation zone characterized by low velocities, high turbulence intensity, and negative pressure. The recirculation zone reduces the effective flow cross-sectional area, thereby accelerating the flow and causing the depth-averaged maximum longitudinal velocity to occur within the contraction region bounded by the recirculation zone boundary and the outerwall (Jin et al., 2023; Schindfessel et al., 2015; Shakibainia et al., 2010).

Crucially, the position of the maximum recirculation zone width deviates from the $\tau_{zx} = 0$ location, causing misalignment between peak velocity and zero-shear stress positions. Figure 10 presents the dimensionless peak velocities ($u_{\max}/u_d$) across cases, revealing a positive correlation with the discharge ratio η. This is because a higher η leads to an expansion of the recirculation zone, thereby enhancing its constrictive effect on the contracted flow and thereby increasing $u_{\max}/u_d$.

5. Calculation of the Depth-Averaged Maximum Longitudinal Velocity

The development of depth-averaged maximum longitudinal velocity is governed by the combined influence of recirculation zone pressure and boundary shear stresses (ice cover and channel bed). However, due to the difficulty in determining the three-dimensional structure of the recirculation zone, the mathematical model developed in this study is designed to estimate the depth-averaged maximum longitudinal velocity in the confluence zone. While the model provides only an approximation, it is sufficiently accurate for most practical engineering applications (Hsu et al., 1998).

Figure 11 illustrates the close agreement between $u_{\max}$ and $u_{\max,re}$ at this cross-section. Their differences are quantified in terms of relative and absolute errors.

$$\varepsilon_u = \frac{|u_{\max,re} - u_{\max}|}{u_{\max}} \times 100\% \tag{14}$$

The absolute error is given as:

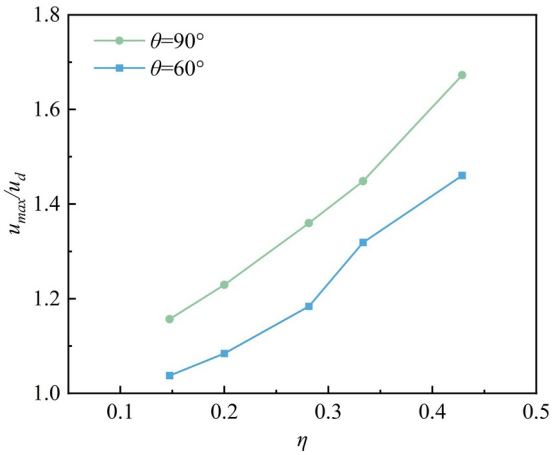

Figure 10. Schematic diagram of the depth-averaged maximum longitudinal velocity variation derived from simulations.

$$\varepsilon_e = |u_{\max,re} - u_{\max}| \tag{15}$$

Error analyses for 90° and 60° junction angles (Table 4) reveal maximum absolute errors of 0.002 m/s (Case B4) and consistent relative errors below 1%. This validates $u_{\max,re}$ as a robust estimator for $u_{\max}$. Further analysis revealed a statistically significant strong positive linear correlation between $u_{\max,re}$ and $u_{\max}$, with a correlation coefficient of $r = 0.999922$ ($p < 0.001$). The very high ($r \approx 1$) r-value and highly statistically significant p-value confirm a clear linear relationship between the two variables. The correlation coefficient and its associated p-value were calculated using the following equations:

$$r = \frac{\sum_{i=1}^{n}(x_i - \bar{x})(y_i - \bar{y})}{\sqrt{\sum_{i=1}^{n}(x_i - \bar{x})^2}\sqrt{\sum_{i=1}^{n}(y_i - \bar{y})^2}} \tag{16}$$

$$p = r\sqrt{\frac{n-2}{1-r^2}} \tag{17}$$

Therefore, $u_{\max,re}$ can be regarded as a reliable estimate of $u_{\max}$. For the 90° junction angle, both ε_e and ε_u are generally higher than those for the 60° confluence. Moreover, as η increases, the deviation between $u_{\max}$ and $u_{\max,re}$ also grows, indicating that a higher lateral momentum ratio leads to a greater discrepancy. Consequently, the maximum depth-averaged recirculation zone width (W_{re}) must be determined prior to deriving the expression for the depth-averaged maximum longitudinal velocity, as detailed in Appendix B.

5.1. Calculation of the Depth-Averaged Maximum Longitudinal Velocity

As depicted in Figure 12, a new Cartesian coordinate system was established with its origin positioned at the boundary of the recirculation zone; the x-axis runs parallel to the main channel wall, while the y-axis is perpendicular to the tangent at the boundary of the maximum width of the recirculation zone. The governing equations are derived from the streamwise Navier-Stokes momentum equation and continuity equation. At the main channel maximum contracted section (MCS), these equations are expressed as:

$$\frac{\partial \tau_{xy}}{\partial y} + \frac{\partial \tau_{xz}}{\partial z} + \rho g S_x = \rho\left(\frac{\partial u^2}{\partial x} + \frac{\partial uv}{\partial y} + \frac{\partial uw}{\partial z}\right) \tag{18}$$

where x, y and z represent the longitudinal, lateral, and vertical directions, respectively; u, v and w represent velocity components in the x, y and z directions, respectively; τ_{xy} and τ_{xz} are the Reynolds shear stresses with respect to the vertical and horizontal planes, expressed as $\tau_{xy} = -\rho u'v'$ and $\tau_{xz} = -\rho u'w'$; ρ denotes the fluid

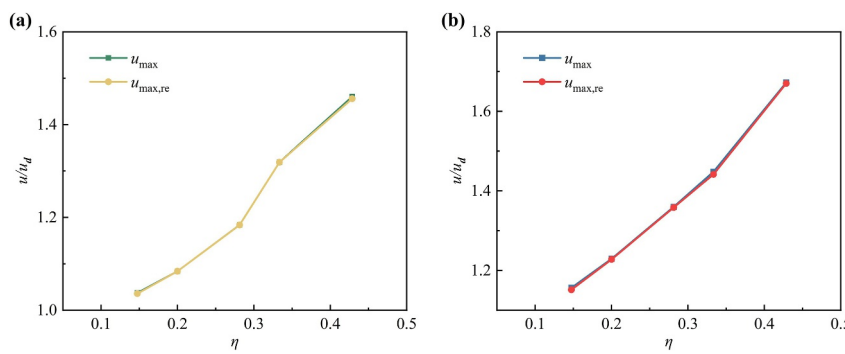

Figure 11. The depth-averaged maximum longitudinal velocity $u_{\max}$ in the confluence versus the depth-averaged maximum cross-sectional flow velocity $u_{\max,re}$ at the largest width of the recirculation zone. (a) Cases at a 60° junction angle; (b) Cases at a 90° junction angle.

Table 4
Error Between u_{max} and $u_{max,re}$ for Different Cases

Case	A1	A2	A3	A4	A5	B1	B2	B3	B4	B5
ε_e (m/s)	0.0005	0	0.00005	0	0.0016	0.0016	0.0005	0.0006	0.002	0.0008
ε_u (%)	0.16	0	0.014	0	0.31	0.44	0.13	0.12	0.47	0.14

density; S_x represents the slope of the riverbed. Integrating Equation 18 over the water depth yields the depth-averaged, two-dimensional momentum equation at the MCS:

$$\rho g h S_x - h\frac{\partial \overline{\tau}_{xy}}{\partial y} - \tau_d = \rho h\left[\frac{\partial (u^2)_d}{\partial x} + \frac{\partial (uv)_d}{\partial y} + \frac{\partial (uw)_d}{\partial z}\right] \tag{19}$$

where $(u^2)_d = \frac{1}{h}\int_0^h (u^2)\,\mathrm{d}z$; $(uv)_d = \frac{1}{h}\int_0^h (uv)\,\mathrm{d}z$; $(uw)_d = \frac{1}{h}\int_0^h (uw)\,\mathrm{d}z$; τ_d is the depth-averaged composite boundary shear stress from the bed and ice cover acting on the constricted flow and $\tau_d = \tau_b + \tau_i$, $\overline{\tau}_{xy}$ is the width-averaged bed and ice cover shear stress acting on the constricted flow, and $\overline{\tau}_{xy} = \frac{1}{h}\int_0^h (-\rho u' v')\,\mathrm{d}z$. In an open channel flow under steady flow, by depth-averaging Equation 16, and noting that the velocity component of w at both the surface and the bottom of channel is zero, Equation 17 becomes as:

$$\rho g h S_x - h\frac{\partial \overline{\tau}_{xy}}{\partial y} - \tau_d = \rho h\left[\frac{\partial (u^2)_d}{\partial x} + \frac{\partial (uv)_d}{\partial y}\right] \tag{20}$$

For MCS under fully developed flow conditions, where it is assumed that $\frac{\partial (u^2)_d}{\partial x} = 0$, Equation 20 becomes:

$$\rho g h S_x - h\frac{\partial \overline{\tau}_{xy}}{\partial y} - \tau_d = \rho h\frac{\partial (uv)_d}{\partial y} \tag{21}$$

In view of the pervasive application of the eddy viscosity approach to numerical modeling, the approach can be utilized to express $\overline{\tau}_{xy}$ as (Shiono & Knight, 1991):

$$\overline{\tau}_{xy} = \rho \overline{\varepsilon}_{xy}\frac{\partial u_v}{\partial y} \tag{22}$$

where u_v is the depth-averaged longitudinal velocity, and $u_v = \frac{1}{h}\int_0^h u\mathrm{d}z$; $\overline{\varepsilon}_{xy}$ is the depth-averaged eddy viscosity, and $\overline{\varepsilon}_{xy} = \lambda_d h u_*$; λ_d is the dimensionless comprehensive eddy viscosity; u_* is the local shear velocity, and $u_* = (\tau_d/\rho)^{0.5} = u_d\,(f_d/8)^{0.5}$; f_d is the Darcy–Weisbach comprehensive friction factor. Thus, the comprehensive boundary shear stress τ_d is expressed as:

$$\tau_d = \rho\frac{f_d}{8}u_v^2 \tag{23}$$

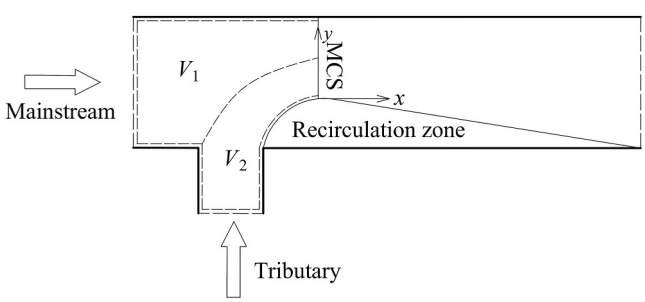

Figure 12. Sketch of the Cartesian coordinate system with x-axis and y-axis, MCS: main channel maximum contracted section.

The occurrence of secondary flow at confluences has been attributed to the unbalance between centrifugal force and pressure gradient forces, which is similar to the generation of secondary flow in meander bends. Therefore, this study adopts the same approach for secondary flow treatment as in curved channels, assuming $u = K_1 u_v$ and $v = K_2 u_v$ (Ervine et al., 2000). Accordingly, Equation 19 can be expressed as:

$$\rho g h S_x - h\frac{\partial \overline{\tau}_{xy}}{\partial y} - \tau_d = \rho h K\frac{\partial u_v^2}{\partial y} \qquad K = K_1 K_2 \tag{24}$$

where K is the secondary flow coefficient. Substituting Equations 22 and 23 into Equation 24 results in:

$$\rho g h S_x - \rho \lambda_d h^2 \frac{\partial}{\partial y}\left(u_v \frac{\partial u_v}{\partial y}\right) - \rho \frac{f_d}{8} u_v^2 = \rho h K \frac{\partial u_v^2}{\partial y} \tag{25}$$

The analytical solution to Equation 25 can be derived as follows:

$$\begin{aligned} u_v &= \sqrt{C_1 e^{r_1 y} + C_2 e^{r_2 y} + \omega} \\ r_1 &= \frac{1}{\lambda_d h}\sqrt{\frac{8}{f_d}}\left(K + \sqrt{K^2 + 2\lambda_d \left(\frac{f_d}{8}\right)^{3/2}}\right) \\ r_2 &= \frac{2K}{\lambda_d h}\sqrt{\frac{8}{f_d}} - r_1 \\ \omega &= \frac{8 g h S_x}{f_d} \end{aligned} \tag{26}$$

where C_1 and C_2 are unknown constants. Within V_1, the boundary shear stress τ_w exerted by the wall on V_1 and the shear force τ_{sh} exerted on the control volume at the interface act in opposing directions, mirroring shear stress conditions found in asymmetric channels (Tsai & Ettema, 1994). Following Einstein's theory of drag separation (Einstein, 1942), V_1 is bisected into two layers by the zero-shear stress position: one influenced by wall shear stress and the other by hypothetical interface shear stress, assuming shear forces are linearly varying. Similarly, in V_2, the shear stress from the recirculation zone opposes that from the hypothetical interface, partitioning V_2 into layers, namely, the interface shear stress layer and the recirculation zone shear stress layer. The lateral depth-averaged shear stresses $\overline{\tau}_{re}, \overline{\tau}_{sh}$ and $\overline{\tau}_b$ in V_1 and V_2 are defined as:

$$\begin{aligned} \overline{\tau}_{xy,V_1} &= \overline{\tau}_w - (\overline{\tau}_w + \overline{\tau}_{sh})\frac{W_1 + W_2 - y}{W_1} \\ \overline{\tau}_{xy,V_2} &= \overline{\tau}_{re} - (\overline{\tau}_{re} + \overline{\tau}_{sh})\frac{y}{W_2} \end{aligned} \tag{27}$$

where $\overline{\tau}_{re}, \overline{\tau}_{sh}$ and $\overline{\tau}_w$ are the depth-averaged shear stress from the recirculation zone, shear layer and wall, respectively, and $\overline{\tau}_{re} = \rho\left(\frac{f_{re}}{8}\right) u_v^2$, $\overline{\tau}_{sh} = \rho\left(\frac{f_{sh}}{8}\right) u_v^2$ and $\overline{\tau}_w = \rho\left(\frac{f_w}{8}\right) u_v^2$, f is the friction coefficient. At the shear layer in the mixing-layer mode, the contracted flow is considered as a single control volume, influenced solely by the transverse shear stress from the recirculation zone and walls. The depth-averaged shear stress $\overline{\tau}_{re}$ and $\overline{\tau}_b$ within V_3 are then expressed as:

$$\overline{\tau}_{xy,V_3} = \overline{\tau}_{re} - (\overline{\tau}_{re} + \overline{\tau}_w)\frac{y}{W_3} \tag{28}$$

In each control volume, it is assumed that the positions where the shear stress, $\overline{\tau}_{xy}$ is zero coincide with the locations of depth-averaged maximum longitudinal velocity within the control volume. Consequently, by substituting $\overline{\tau}_{xy} = 0$ into Equations 27 and 28 the positions of depth-averaged maximum longitudinal velocity in V_1, V_2 and V_3 are expressed as:

$$\begin{aligned} y_1' &= W_1 + W_2 - \frac{\overline{\tau}_w}{\overline{\tau}_w + \overline{\tau}_{sh}} W_1 \\ y_2' &= \frac{\overline{\tau}_{re}}{\overline{\tau}_{re} + \overline{\tau}_{sh}} W_2 \\ y_3' &= \frac{\overline{\tau}_{re}}{\overline{\tau}_{re} + \overline{\tau}_w} W_3 \end{aligned} \tag{29}$$

When the shear layer at the cross-section corresponding to the maximum depth-averaged width of the recirculation zone is in the wake mode, Equation 26 is applied to the MCS of control volumes V_1 and V_2. When the shear layer at this cross-section is in the mixing-layer mode, Equation 26 is applied to the MCS of control volume V_3. Combining Equation 29 with Equation 26. This allows the calculation of the depth-averaged maximum longitudinal velocity ($u_{\max,re}$) at the MCS for each mode and each control volume, which serves as an approximation of the depth-averaged maximum longitudinal velocity ($u_{\max}$).

5.2. Boundary Conditions and Coefficients

5.2.1. Boundary Conditions

To solve Equation 26, appropriate boundary conditions must be imposed on the unknown variables. The integration constants C_1–C_3 are determined by substituting velocity profiles at arbitrary locations within each control volume. Solution accuracy improves when selected points approach the depth-averaged maximum longitudinal velocity location. For the results presented in Section 6, boundary conditions were specified at midpoints between the depth-averaged maximum longitudinal velocity position and lateral boundaries in each control volume (V_1, V_2, and V_3), with velocity data extracted from numerical simulations.

5.2.2. Dimensionless Comprehensive Eddy Viscosity λ_d

Research on the dimensionless eddy viscosity coefficient (λ_d) has primarily focused on trapezoidal channels, open channels, and compound river systems, with limited studies addressing its values in ice-covered confluences. The adoption of depth-averaged momentum equations in the modeling framework reduces the 3D system to 2D, applying the depth-averaged contraction coefficients to compute the effective flow width at the MCS. Consequently, employed the established λ_d value for rectangular ice-covered channels in this study, $\lambda_d = 0.067$ (Zhong et al., 2019).

5.2.3. Friction Factor

For the combined boundary shear stress τ_d caused by the bed and ice cover, the friction coefficient is formulated based on the relationship between bed shear stress and ice cover shear stress. That is $\tau_d = \tau_i + \tau_b$, where τ_i and τ_b denote the shear stresses exerted by the ice cover and bed on the contracted flow, respectively. Considering, $\tau_i = \rho(f_i/8)\,u_v^2$ and $\tau_b = \rho(f_b/8)\,u_v^2$, we have:

$$\tau_d = \rho\left(\frac{f_d}{8}\right)u_v^2 = \rho\left(\frac{f_i}{8}\right)u_v^2 + \rho\left(\frac{f_b}{8}\right)u_v^2 \tag{30}$$

where f_i and f_b are the Darcy-Weisbach friction coefficients for the ice cover and bed, respectively. The force balance within each control volume is analogous to that in ice-covered straight channels. Numerous models have derived expressions for these friction factors. The expressions adopted in the present mathematical model are given below, with detailed derivations provided in Appendix C.

$$\begin{aligned} f_w &= \frac{8gn_w^2}{\left(\frac{W_1 n_b^{3/2}}{n_w^{3/2}+n_{sh}^{3/2}}\right)^{1/3}} \\ f_{re,V_2} &= \frac{8gn_{re,V_2}^2}{\left(\frac{W_2 n_b^{3/2}}{n_{re,V_2}^{3/2}+n_{sh}^{3/2}}\right)^{1/3}} \\ f_{re,V_3} &= \frac{8gn_{re,V_3}^2}{\left(\frac{W_3 n_{re,V_3}^{3/2}}{n_w^{3/2}+n_{re,V_3}^{3/2}}\right)^{1/3}} \end{aligned} \tag{31}$$

where n represents the roughness coefficient, n_{re} and n_{sh} are experimentally determined via logarithmic velocity profile fitting at any cross-section.

Table 5
Parameter Statistics Table

Case	A1	A2	A3	A4	A5	B1	B2	B3	B4	B5
Model	Wake model	Mixing-layer model	Mixing-layer model	Mixing-layer model	Mixing-layer model	Mixing-layer model	Mixing-layer model	Mixing-layer model	Mixing-layer model	Mixing-layer model
n_b	0.016	0.016	0.016	0.016	0.016	0.016	0.016	0.016	0.016	0.016
n_w	0.016	0.016	0.016	0.016	0.016	0.016	0.016	0.016	0.016	0.016
n_i	0.0177	0.0177	0.0177	0.0177	0.0177	0.0177	0.0177	0.0177	0.0177	0.0177
n_{sh}	0.00351	\	\	\	\	\	\	\	\	\
n_{re}	0.001	0.00844	0.00801	0.00978	0.0117	0.00775	0.00927	0.0104	0.0123	0.0154
K	0.013	0.015	0.039	0.029	0.076	0.01	0.016	0.014	0.034	0.017

5.2.4. Secondary Flow Coefficient K

Two distinct secondary flows formed at the confluence alter the velocity and shear stress distributions (Shen et al., 2022). This study employs the secondary flow coefficient K to quantify its influence on longitudinal velocity, where K is relative to the number, rotational direction, and strength of secondary current cells (Wang et al., 2020). As the junction angle increases, both secondary flow strength within the cross-section due to enhanced centrifugal forces and greater lateral pressure gradients at larger angles (Shen et al., 2022; Yuan, Xu, et al., 2022). Downstream evolution reveals that with the gradual replenishment and superposition mixing of the vertical flow, the strength of the secondary flow gradually decreases until it disappears (Bradbrook et al., 2000; Chen et al., 2017). These complexities pose challenges for the direct determination of the K value at the MCS. Assuming a uniform K value across the MCS cross-section, the K value can be inversely calculated by substituting depth-averaged flow velocity data from a single point within the control volume into Equation 24. The accuracy of the estimated K value can be further improved by incorporating additional experimental data points. The influence of K variations in the secondary flow coefficient on the depth-averaged maximum longitudinal velocity will be analyzed in the subsequent discussion section.

6. Result

To validate the effectiveness and reliability of the proposed models, the results calculated by the models were compared to the simulated results. Since this paper does not involve the physical analysis of the flow characteristics in the recirculation zones, the boundary location of the recirculation zone is determined using the simplified zero-unit-discharge method proposed by Schindfessel et al. (2017). In the zero-unit-discharge method, it is assumed that the discharge across the cross-section of the recirculation zone is zero. The local width of the horizontal recirculation zone at a specified height (z) and cross-sectional position (x) above the riverbed (denoted as $W_{re}(x,z)$) is defined as the flow corresponding to a unit height, obtained by integrating the longitudinal flow velocity component (u) laterally from the inner bank to the outer bank. When the resulting integral equals zero, the discharge within the width at that height is considered to be zero. Hence, the value of $W_{re}(x,z)$ represents the width of the recirculation zone at the position (x, z), This condition is mathematically expressed as:

$$\int_0^{W_{re}(x,z)} u(x,y,z)\,\mathrm{d}y = 0 \tag{32}$$

The parameters required for the calculations are presented in Table 5. As shown in Table 5, the values of n_{re} and n_{sh} are not constant. Specifically, significant variability is observed in the values of n_{re}, while data for n_{sh} are limited due to the infrequent occurrence of wake modes under the studied flow conditions. If the apparent roughness is assumed to reflect the influence of turbulent structures, the observed variations in these values may be explained by the presence of intense turbulence near the boundaries of the recirculation zone and within the shear layer—a region characterized by the advection of large-scale coherent structures (Rhoads & Sukhodolov, 2001, 2004; Sukhodolov & Rhoads, 2001). Crucially, under mixed-flow conditions, the value of n_{re} for a junction angle of 60° is consistently lower than that for a 90° angle. This difference arises directly from the formation of significantly larger and more dynamically intense recirculation zones at the larger (90°) junction

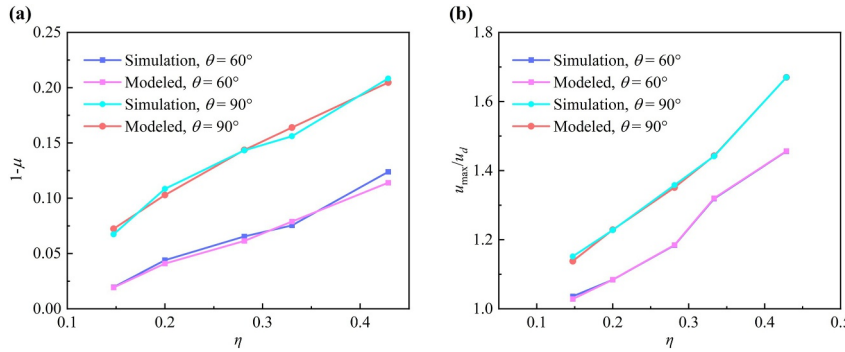

Figure 13. Comparison of model predictions versus numerical simulations; (a) maximum depth-averaged recirculation zone width; (b) depth-averaged maximum longitudinal velocity.

angles. These larger recirculation zones are associated with stronger adverse pressure gradients and enhanced flow reversal near the channel boundaries. This intensified flow reversal and the associated stronger shear significantly amplify turbulence production along the boundaries of these recirculation zones, thereby increasing the apparent roughness (n_{re}) and its observed variability. This can also explain the observed increase in the roughness coefficient (n_{re}) with increasing discharge ratio under identical confluence angles. Simultaneously, the deformability of the ice cover itself increases the complexity and variability of these interactions, inherently limiting the accuracy of an analytical expression for the roughness coefficient.

Before validating the depth-averaged maximum longitudinal velocity, the accuracy of Equation B5 (maximum depth-averaged recirculation zone width) must first be verified. Figure 13a provides comparative plots of the calculated versus simulated results for Equation B4. Equation B4 exhibits a maximum relative error of 8.7% and a peak absolute deviation of 0.009 in Case A5. Crucially, relative errors remain below 10% across all validation cases, confirming the equation's accuracy and demonstrating its robustness for the studied conditions.

The relative and absolute errors between the calculated and simulated values were determined using Equations 14 and 15, respectively, and the resulting errors are summarized in Table 6. Absolute errors range from 0.0003 to 0.0011 m/s, while relative errors span 0.03%–1.61%, both peaking in Case B1. Case A2 exhibits the highest precision. These error metrics confirm the model's capability to predict maximum depth-averaged longitudinal velocities at 60° and 90° junction angles in channel confluences. Furthermore, a comparative analysis of the predictive accuracy between the depth-averaged maximum longitudinal velocity calculated using the mass-conservation method and the present semi-analytical model is provided in Appendix D. The results demonstrate that the predictive accuracy of our model is significantly higher than that of the simplified approach.

7. Discussion

7.1. Secondary Flow Coefficient *K*

The secondary flow coefficient serves as a primary controlling parameter in the semi-analytical model; however, its accurate, mathematical determination remains challenging. Under the present experimental conditions, all obtained *K* values were positive (0.01–0.076), indicating that a clockwise-rotating secondary circulation dominated in the confluence zone. At a constant junction angle, *K* increased with the discharge ratio, suggesting that the greater lateral momentum flux introduced by the tributary flow generated enhanced centrifugal forces. Conversely, under a constant discharge ratio, *K* decreased as the junction angle increased due to the influence of the recirculation zone: a larger junction angle leads to a wider recirculation zone, which in turn decreases the

Table 6
Error Statistics of the Depth-Averaged Maximum Longitudinal Velocity

Case	A1	A2	A3	A4	A5	B1	B2	B3	B4	B5
ε_a (m/s)	0.003	0.0001	0.0003	0.0003	0.0013	0.00592	0.0003	0.0029	0.0017	0.00092
ε_r (%)	0.90	0.036	0.067	0.074	0.26	1.62	0.077	0.64	0.39	0.16

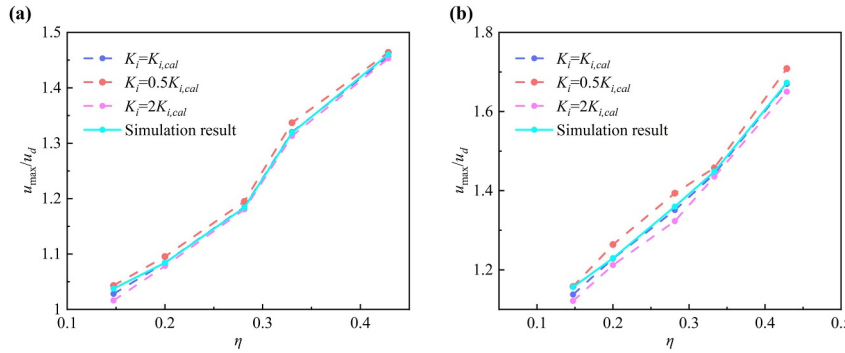

Figure 14. Effects of coefficients K on depth-averaged maximum longitudinal velocity distributions.

effective flow area. This increase decreases the K_2 term in Equation 24, ultimately resulting in a lower overall K value. The relationships identified between K and key hydraulic/geometric parameters (discharge ratio, junction angle) provide valuable insights and a foundation for developing future predictive methods for a priori estimating K.

Figure 14 presents a systematic sensitivity analysis of the secondary flow coefficient (K_i) across all investigated cases. We varied the coefficient between 0.5 and 2.0 times its calibrated value ($K_{i,cal}$) while holding other parameters constant (Table 5). Figure 14 demonstrates that increasing K_i reduces predicted values, whereas decreasing K_i elevates them. Cases with 90° junction angles exhibit greater sensitivity to K_i variations than those at 60°. Crucially, however, K_i adjustments exert minimal influence on computed results, confirming that ice cover and bed shear stresses and recirculation zone compression remain the dominant factors governing depth-averaged maximum longitudinal velocity.

7.2. Empirical Coefficient φ

In this study, the empirical coefficient φ is introduced into Equation 12 to correct for the influence of secondary flow on the position of the shear layer. When the shear layer is in wake mode, this coefficient determines the zero-shear stress location (and thus the depth-averaged maximum longitudinal velocity location in Equation 27). Based on the experimental and numerical data presented, the value of φ is determined to be 0.04. Omitting φ from Equation 12 would cause an overestimation of the effective flow area (W_1) in control volume V_1 and an underestimation of the corresponding area (W_2) in V_2. This would shift the predicted location of the depth-averaged maximum longitudinal velocity toward the inner bank (see Equation 27). For constant secondary flow coefficient and friction coefficients, subsequent prediction via Equation 24 would overestimate the depth-averaged maximum longitudinal velocity in V_1 and underestimate it in V_2. It should be noted that, due to the limited range of conditions investigated, a generalized calculation method for φ requires future quantification through scaled flume experiments or field measurements.

7.3. Limitations of the Model and Future Developments

This study proposes semi-analytical models to calculate u_{max} using the control volume method. The models do not directly calculate u_{max}, but they target $u_{max,re}$, which is proximate to u_{max}. This approach addresses the difficulty of capturing the exact location of u_{max}, making it possible to calculate u_{max}. Compared to a numerical model, the semi-analytical model developed in this study achieves a substantial improvement in computational efficiency. Notably, this approach eliminates the need for grid generation, significantly reducing setup time and ensuring that accuracy remains independent of grid properties such as size or shape. For many engineering applications, simulating the complete three-dimensional flow field within a channel is not strictly needed, while the estimation of the depth-averaged maximum longitudinal velocity or maximum width of the separation/recirculation zone is enough. It is noteworthy that the semi-analytical model derives a formula for depth-averaged maximum longitudinal velocity, providing approximate guidance for maximum longitudinal velocity in confluence zones. For practical engineering applications, however, this level of precision proves adequate.

The choice between a single or dual control-volume model for calculating u_{max} depends on the mixing mode of the shear layer at the cross-section of the maximum recirculation zone width. This mode can be determined using either the theoretical model proposed by Sukhodolov et al. (2023) for describing shear layer mixing processes or through mixed dye visualization experiments (Sukhodolov & Rhoads, 2001). It is important to note that while the theoretical model by Sukhodolov et al. (2023) was developed for open channels, it can be adapted for ice-covered confluence channels by applying the two-layer assumption (Einstein, 1942). The primary distinction between open and ice-covered channels lies in the source of shear stress: in the former, only bed shear stress is found, whereas in the latter, a combined ice cover and bed shear stress is acting. Consequently, the bed shear stress parameter in the original theoretical model should be replaced with the expression for the combined boundary shear stress provided in Appendix C.

This semi-analytical model is tailored for two specific junction angles, whereas natural confluences exhibit a wide spectrum of angles, constraining its broader applicability. However, in confluences with smaller θ (e.g., 30°), the depth-averaged maximum longitudinal velocity was lower because smaller junction angles typically result in a significantly narrower or non-existent recirculation zone, thereby minimizing the depth-averaged maximum longitudinal velocity effect that would otherwise arise from the reduction in the effective flow cross-section. To enhance the model's generalizability, future work will focus on deriving a more accurate expression for ζ through experimental data covering an extended range of junction angles (θ).

The mathematical models developed are based on the laboratory-scale confluence channel, including sharp junction angles and rectangular cross-sections. As the derivation process of the semi-analytical models does not account for the effects of bed discordance and velocity-dip phenomena, changes in conditions (such as trapezoidal cross-section or smooth junction angle) may compromise their prediction accuracy (Li et al., 2025; Yuan, Yan, et al., 2023, 2024). Therefore, when extending the model to large-scale natural river confluences, its applicability requires further validation. Integrating additional hydrological data will help test and enhance this applicability.

8. Conclusion

To investigate hydrodynamic characteristics in confluent channels, this study examines factors influencing maximum longitudinal velocity. By applying the control volume approach and momentum equation, a semi-analytical model for calculating maximum depth-averaged longitudinal velocities at confluences is developed. The model was validated against numerical simulations.

1. A novel interface position was established at the minimum-velocity location within the shear layer, incorporating effects of junction angle, discharge ratio, and secondary flows.
2. Depth-averaged maximum longitudinal velocity was characterized at sections with maximum recirculation zone width, simplifying the solution process. Relative error analysis revealed a mean deviation of 0.18% between approximated and simulated values, demonstrating the method's efficacy.
3. The dual-mode behavior of the shear layer was accounted for, with the secondary flow coefficient introduced to quantify its influence on depth-averaged maximum longitudinal velocity.

Although this work presents an effective mathematical framework for computing maximum depth-averaged longitudinal velocities, future studies could further refine the approach, particularly by deriving analytical solutions for the secondary flow coefficient K and determining the range of the empirical coefficient φ through further experimental studies or numerical simulations.

Appendix A

A grid sensitivity analysis targeting the downstream confluence velocity field—critical to recirculation zone delineation—was conducted using three mesh configurations:

Medium mesh: 4.9 million cells (1.3 × 1.3 × 10 mm);
Fine mesh: 9.7 million cells (0.7 × 0.7 × 10 mm);
Coarse mesh: 2.4 million cells (4 × 4 × 10 mm).

Velocity profiles along the longitudinal transect $y = 0.5$ m, $z = 0.125$ m revealed negligible differences between fine mesh and medium mesh (Figure A1), and the Grid Convergence Index (GCI) for the medium mesh measured 2.29% (<3% threshold; Celik et al., 2008), demonstrating grid independence.

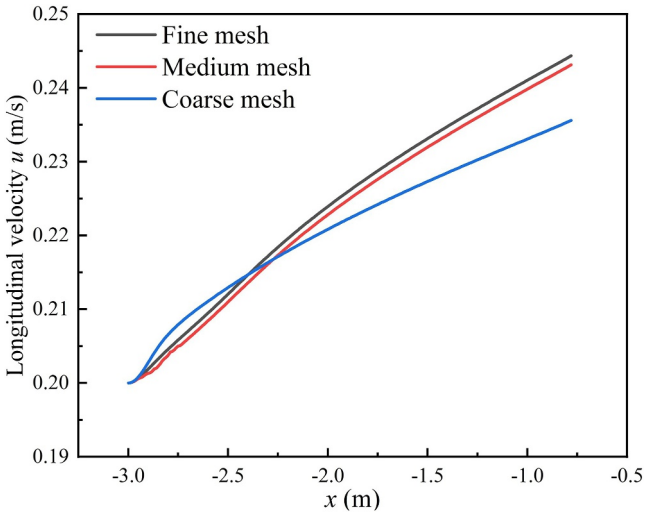

Figure A1. Comparison of the longitudinal distribution of the velocity for coarse, medium, and fine mesh.

Appendix B

This appendix details a mathematical model for calculating the maximum depth-averaged width of the recirculation zone. The governing equations are derived based on the conservation of momentum, energy, and mass, incorporating an expression for the average hydrodynamic pressure on the sidewall of the tributary channel. This pressure term is determined from the hydrostatic pressure difference between the inner and outer banks of the tributary. Empirical coefficients in the model are subsequently calibrated using experimental data.

B1. Determination of the Maximum Depth-Averaged Recirculation Zone Width

The maximum recirculation zone width, governed by junction angle θ and discharge ratio η, has been validated through experimental measurements, numerical simulations, and analytical formulations. As depicted in Figure B1, a Cartesian coordinate system is established with its origin at the midpoint of the Tributary Downstream Section (TDS), where the n-axis aligns with the TDS centerline. At the cross-section of maximum recirculation width, the effective flow width of control volumes is conventionally assumed to be bounded by the recirculation zone interface and the outerwall (MCS), with flow direction parallel to the sidewall at this section. Based on mass conservation principles, the relationship between effective flow area and mean velocity is derived as:

$$Q_{\mathrm{MCS}} = h_{\mathrm{MCS}} W_{\mathrm{MCS}} u_{\mathrm{MCS}} = \mu W_d h_{\mathrm{MCS}} u_{\mathrm{MCS}} \tag{B1}$$

where Q_{MCS} is the discharge through the MCS; μ is the maximum flow contraction coefficient given by $\mu = W_{\mathrm{MCS}}/W_d$; u_{MCS} is the average cross-sectional flow velocity along the direction of s-axis at the MCS. Due to the ice cover presence, the free surface is modeled as a rigid-lid boundary with constant water depth h throughout the confluence zone. The relationship between μ, θ, and η is determined by formulating energy and momentum equations for a control volume bounded by MCS, the tributary upstream section (TUS), and the main channel upstream section (MUS). The energy conservation equation for this control volume is expressed as:

$$\left(h_{\mathrm{TUS}} + \frac{\alpha_{\mathrm{TUS}} Q_{\mathrm{TUS}}^2}{2gA_{\mathrm{TUS}}^2}\right) Q_{\mathrm{TUS}} + \left(h_{\mathrm{MUS}} + \frac{\alpha_{\mathrm{MUS}} Q_{\mathrm{MUS}}^2}{2gA_{\mathrm{MUS}}^2}\right) Q_{\mathrm{MUS}} = \left(h_{\mathrm{MCS}} + \frac{\alpha_{\mathrm{MCS}} Q_{\mathrm{MCS}}^2}{2gA_{\mathrm{MCS}}^2}\right) Q_{\mathrm{MCS}} \tag{B2}$$

where A is the effective cross-sectional area of the channel given by $A = hW$; assuming the upstream water depths are equal (Creelle et al., 2016; Hager, 1987), namely $h_{\mathrm{TUS}} = h_{\mathrm{MUS}}$; Q is the discharge through the effective cross-section; α is the energy correction coefficient. Accounting for tributary flow deflection prior to confluence and neglecting interfacial shear stresses at ice cover and bed boundaries, the momentum equation for the control volume bounded by MCS, TUS, and MUS is formulated as:

$$\frac{\beta_{\mathrm{TUS}} Q_{\mathrm{TUS}}^2}{g h_{\mathrm{TUS}} W_{\mathrm{TUS}}} \cos(\theta') + \frac{1}{2} h_{\mathrm{TUS}}^2 W_{\mathrm{TUS}} \cos(\theta') + \frac{1}{2} h_{\mathrm{MUS}}^2 W_{\mathrm{MUS}} + \frac{\beta_{\mathrm{MUS}} Q_{\mathrm{MUS}}^2}{g h_{\mathrm{MUS}} W_{\mathrm{MUS}}}$$
$$= \frac{\beta_{\mathrm{MCS}} Q_{\mathrm{MCS}}^2}{g h_{\mathrm{MCS}} W_{\mathrm{MCS}}} + \frac{1}{2} h_{\mathrm{MCS}}^2 W_{\mathrm{MCS}} + \frac{P^*}{\rho g} h_{\mathrm{TUS}} W_{\mathrm{TUS}} \sin(\theta') \tag{B3}$$

where β is the momentum correction coefficient; θ' is the flow junction angle at the TDS as shown in Figure B1, P^* is the average hydrodynamic pressure exerted on the side walls of the tributary channel, calculated as P_{TIW}-P_{TOW}, where P is the hydrostatic pressure, TIW and TOW are the inner and outer banks of the branch channel respectively, as shown in Figure B1.

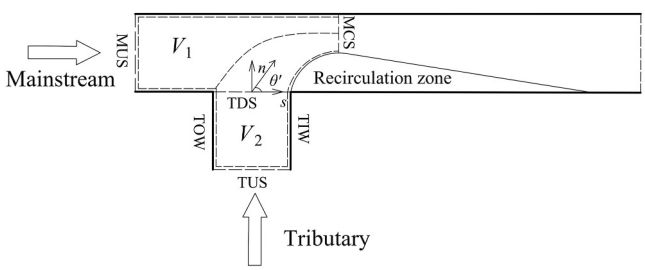

Figure B1. Schematic diagram of the n-axis and s-axis Cartesian coordinate system and naming convention for cross-sections and walls; TDS: tributary downstream section; TUS: tributary upstream section; MUS: main channel upstream section.

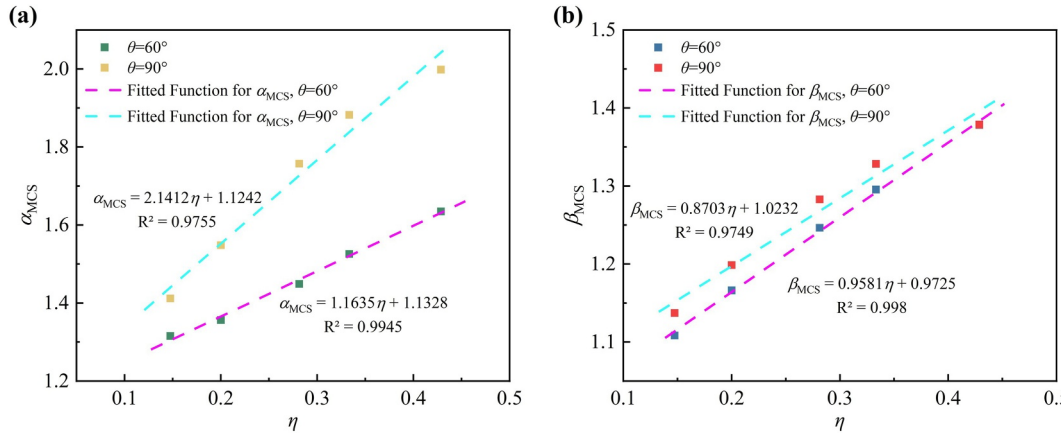

Figure B2. Variation of (a) α_{MCS} and (b) β_{MCS} with discharge ratio.

Hager (1987) posited that P^* solely correlates with the pressures at the TUS and MCS, thereby P^* can be articulated as:

$$P^* = \frac{P_{TUS} + \zeta P_{MCS}}{1+\zeta} = \frac{1}{2}\rho g \frac{h_{TUS} + \zeta h_{MCS}}{1+\zeta} \tag{B4}$$

where ζ is a dimensionless parameter. Upon synthesizing Equation B2 and B3, one can ascertain the relationship among μ, η and θ'. The maximum flow contraction coefficient is delineated as (Hager, 1987):

$$\mu = \frac{\alpha_{MCS}\left(1 + Y + \frac{\zeta \sin(\theta')}{1+\zeta}\overline{W}Y\right)}{2\beta_{MCS} + \sqrt{4\beta_{MCS}^2 - \alpha_{MCS}\left[1 + \frac{1}{Y} + \frac{\zeta \sin(\theta')}{1+\zeta}\overline{W}\right]\left\{4\beta_{MUS}(1-\eta)^2 + 4\beta_{TUS}\eta^2\cos(\theta')/\overline{W} - \left[1 + \frac{1}{Y} + \overline{W}\frac{\zeta \sin(\theta')}{1+\zeta}\right]\left[\alpha_{MUS}(1-\eta)^3 + \alpha_{TUS}\eta^3/\overline{W}^2\right]\right\}}} \tag{B5}$$

where $\overline{W}$ is the width ratio, defined as $\overline{W} = W_{TUS}/W_{MUS}$, Y is the depth ratio, defined as $Y = h_{MUS}/h_{MCS}$, Under the constant-depth assumption, namely $Y = 1$.

B2. Energy Coefficient and Momentum Coefficient

The magnitudes of the energy coefficient in Equation B2 and the momentum coefficient in Equation B3 depend on the junction angle and discharge ratio, and evolve as the flow develops downstream. These coefficients peak at the location of the maximum recirculation zone width. At the upstream sections (MUS, TUS), both coefficients are assumed to be unity, namely $\alpha_{MUS} = \alpha_{TUS} = \beta_{MUS} = \beta_{TUS} = 1$ (Hsu et al., 1998; Luo et al., 2018). Figure B2 presents the momentum and energy correction coefficients calculated at the MCS from numerical model results across all test cases. The energy and momentum coefficients, α_{MCS} and β_{MCS}, are calculated by numerically integrating over the cross-section using the velocity u at cell centers, using the following approach (Luo et al., 2018):

$$\alpha = \frac{\int_A u^3 dA}{u_d^3 A} = \frac{\sum_{i,j} u_{i,j}^3 A_{i,j}}{u_d^3 \sum_{i,j} A_{i,j}} \tag{B6}$$

$$\beta = \frac{\int_A u^2 dA}{u_d^2 A} = \frac{\sum_{i,j} u_{i,j}^2 A_{i,j}}{u_d^2 \sum_{i,j} A_{i,j}} \tag{B7}$$

where $A_{i,j}$ is the grid area. The energy coefficient exhibits a greater range of variation than the momentum coefficient. Specifically, the energy coefficient ranges from 1.3 to 1.99, while the momentum coefficient ranges from 1.1 to 1.37. The values of α and β increase linearly with increasing junction angle and discharge ratio, attributable to the enhanced three-dimensionality of the flow field. For the practical determination of these

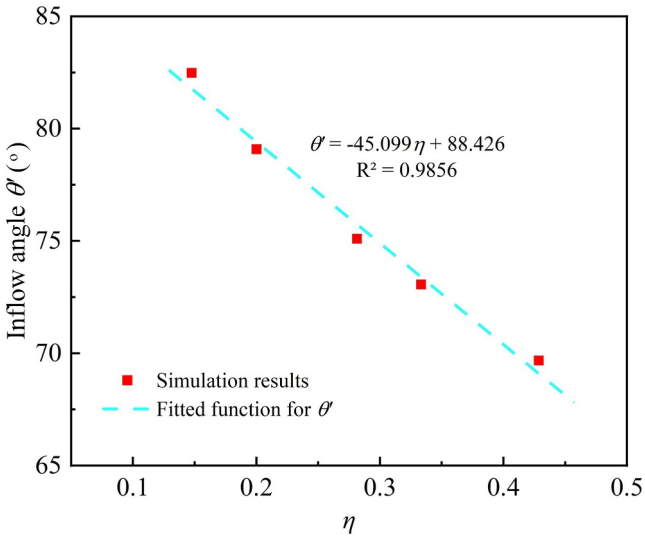

Figure B3. Depth-averaged flow angle θ' across the branch channel entrance at 90° confluence.

coefficients in Equation B5, this study recommends employing the following empirical equations, which are also used to generate the results presented in Section 6.

$$\begin{cases} \alpha_{MCS} = 1.1635\eta + 1.1328, \theta = 60° \\ \alpha_{MCS} = 2.1412\eta + 1.1242, \theta = 90° \end{cases} \tag{B8}$$

$$\begin{cases} \beta_{MCS} = 0.958\eta + 0.9725, \theta = 60° \\ \beta_{MCS} = 0.8703\eta + 1.0232, \theta = 90° \end{cases} \tag{B9}$$

B3. Inflow Angle θ'

Numerous studies indicate that tributary flow deflects before entering the main channel, resulting in an inflow angle θ' in Equation B3 that differs from the geometric junction angle. This deflection increases with both the junction angle and the discharge ratio, becoming pronounced at 90°. Figure B3 shows the tributary inflow angle for the 90° confluence case. Assuming no pre-entry deflection occurs at a 60° junction angle, namely $\theta' = 60°$, and propose the following empirical equation to calculate the deflection angle θ' for 90° confluence, which is expressed as:

$$\theta' = -45.099\eta + 88.426 \tag{B10}$$

B4. Dimensionless Parameter ζ

The dimensionless parameter ζ, which governs P^* in Equation B4, exhibits dependencies on both η and θ. For open-channel confluences, P^* gradually decreases as η increases—corresponding to an increase in ζ—and is typically greater at a junction angle (θ) of 90° than at 60°. This trend arises because increasing η or decreasing θ reduces tributary flow deflection (Creelle et al., 2016; Hager, 1989), thereby diminishing the water depth difference along the sidewall and causing P^* to decrease. In ice-covered channels, however, ζ follows a distinct trend due to the rigid-lid effect at the water surface. Values of ζ across all cases, computed from numerical simulations, as shown in Figure B4, reveal fitted functions and correlations between ζ and η at constant θ. The empirical expression derived from fitting procedures is described below:

$$\begin{cases} \zeta = -18.285\eta^2 + 15.243\eta - 1.6524, \theta = 60° \\ \zeta = -1.2222\eta - 0.2097, \theta = 90° \end{cases} \tag{B11}$$

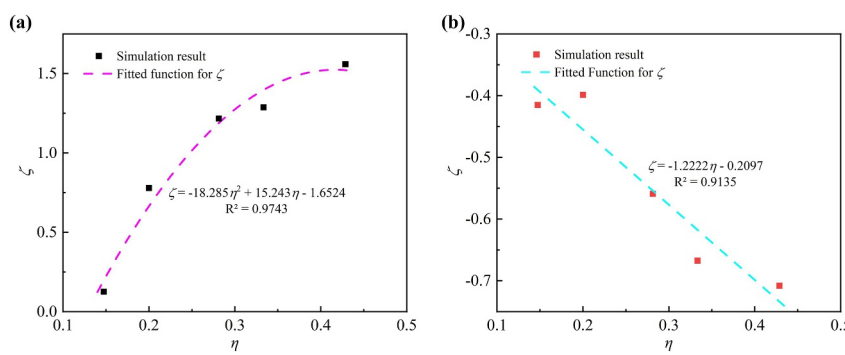

Figure B4. Variation of ζ with discharge ratio, (a) 60° confluence; (b) 90° confluence.

Appendix C

This appendix details the derivation of the friction coefficients f_i, f_b. f_{re}, f_w and f_{sh}. These coefficients are used to calculate the combined shear stress τ_d (Equation 30) and determine the locations of depth-averaged maximum longitudinal velocity $\dot{y}_1$, $\dot{y}_2$, and $\dot{y}_3$ (Equation 29). τ_i and τ_s reach their maximum values at the ice cover and bed boundaries, respectively, and also have opposite directions. According to Einstein's resistance theory (Einstein, 1942), the effective cross-sectional area can be divided into distinct layers associated with different boundary shear stresses. For the combined boundary shear stress τ_b, the effective cross-section is divided into shear stress regions dominated by the bed and ice cover. The composite friction coefficient f_d is defined as follows:

$$f_d = \frac{\chi_i f_i + \chi_b f_b}{\chi_i + \chi_b} \tag{C1}$$

where χ_i and χ_b represent the dimensionless wetted perimeter of the ice cover and the bed per unit height, respectively, both equal in magnitude to depth-average effective cross-section width, that is, $\chi_i = \chi_s = \mu W_d$. The friction coefficients f_i, f_b. f_{re}, f_w and f_{sh} can be calculated by combining the Chezy formula with the Manning equation. From this, the friction coefficients can be expressed as:

$$f_i = \frac{8gn_i^2}{R_i^{1/3}} \tag{C2}$$

$$f_b = \frac{8gn_b^2}{R_b^{1/3}} \tag{C3}$$

$$f_{re} = \frac{8gn_{re}^2}{R_{re}^{1/3}} \tag{C4}$$

$$f_w = \frac{8gn_w^2}{R_w^{1/3}} \tag{C5}$$

$$f_{sh} = \frac{8gn_{sh}^2}{R_{sh}^{1/3}} \tag{C6}$$

where n is the roughness coefficient, n_{re} and n_{sh} are experimentally determined via logarithmic velocity profile fitting at any cross-section; R is the hydraulic radius. Based on the expression for the composite friction coefficient derived by Wang et al. (2020) in ice-covered channels, the expression for f_d is obtained as:

$$f_d = \frac{8g}{\chi_i + \chi_b}\left[\frac{n_i^{3/2} + i_1 n_b^{3/2}}{(1+i_1)R_d}\right]^{1/3}\left(\chi_i n_i^{3/2} + \chi_b n_b^{3/2}\right) \tag{C7}$$

where i_1 is the ratio of χ_b to χ_i, namely $i_1 = \chi_b/\chi_i = 1$; R_d is the composite hydraulic radius, and $R_d = h/2$. Using the Chezy formula and the Manning equation, the expressions for the depth-averaged streamwise velocities in the recirculation zone shear stress layer, the wall shear stress layer, and the hypothetical interface shear stress layer are derived as follows:

$$\begin{aligned} \overline{u}_w &= \frac{R_w^{2/3} J_w^{1/2}}{n_w} \\ \overline{u}_{re} &= \frac{R_{re}^{2/3} J_{re}^{1/2}}{n_{re}} \\ \overline{u}_{sh} &= \frac{R_{sh}^{2/3} J_{sh}^{1/2}}{n_{sh}} \end{aligned} \tag{C8}$$

where J is the hydraulic slope of each shear stress layer; $\overline{u}$ is the average flow velocity in each shear stress layer. Utilizing the common assumptions in asymmetric channels (Ervine et al., 2000), specifically within V_1, $\overline{u}_w = \overline{u}_{sh,V_1}$, $J_w = J_{sh,V_1}$ and within V_2, $\overline{u}_{re} = \overline{u}_{sh,V_2}$, $J_{re} = J_{sh,V_2}$. Accordingly, combining Equation C7 the relationship between R_{w,V_1} and R_{sh,V_1}, as well as those between R_{re,V_2} and R_{sh,V_2} can be present as

$$\begin{aligned}\frac{R_{w,V_1}}{R_{sh,V_1}} &= \frac{n_w^{3/2}}{n_{sh}^{3/2}} \\ \frac{R_{re,V_2}}{R_{sh,V_2}} &= \frac{n_{re,V_2}^{3/2}}{n_{sh}^{3/2}}\end{aligned} \tag{C9}$$

The comprehensive hydraulic radius R_{V_1} within V_1 and the comprehensive hydraulic radius R_{V_2} within V_2 are represented as:

$$\begin{aligned}R_{V_1} &= \frac{A_w + A_{sh}}{\chi_w + \chi_{sh}} = \frac{(A_w/\chi_w)\chi_w/\chi_{sh} + A_{sh}/\chi_{sh}}{1 + \chi_w/\chi_{sh}} = \frac{i_2 + n_{sh}^{3/2}/n_w^{3/2}}{1 + i_2} R_{w,V_1} \\ R_{V_2} &= \frac{A_{re,V_2} + A_{sh}}{\chi_{re,V_2} + \chi_{sh}} = \frac{(A_{re,V_2}/\chi_{re,V_2})\chi_{re,V_2}/\chi_{sh} + A_{sh}/\chi_{sh}}{1 + \chi_{re,V_2}/\chi_{sh}} = \frac{i_2 + n_{sh}^{3/2}/n_{re,V_2}^{3/2}}{1 + i_2} R_{re,V_2}\end{aligned} \tag{C10}$$

where χ_w, χ_{sh} and χ_{re,V_2} are respectively the dimensionless wetted perimeters of the wall per unit depth, the hypothetical interface per unit depth and the recirculation zone per unit depth. At the MCS, χ_w and χ_{re,V_2} can be taken as χ_{sh}, namely $i_2 = 1$. Based on Equation C10, we get:

$$\begin{aligned}R_{w,V_1} &= \frac{2}{1 + n_{sh}^{3/2}/n_w^{3/2}} R_{V_1} \\ R_{re,V_2} &= \frac{2}{1 + n_{sh}^{3/2}/n_{re,V_2}^{3/2}} R_{V_2}\end{aligned} \tag{C11}$$

The comprehensive hydraulic radius within V_1 and V_2 are equal to half the width of the shear stress layer, that is, $R_{V_1} = W_1/2$, $R_{V_2} = W_2/2$, thus, the hydraulic radius of the wall shear stress layer and the hydraulic radius of the recirculation shear stress are defined as:

$$\begin{aligned}R_{w,V_1} &= \frac{W_1 n_w^{3/2}}{n_w^{3/2} + n_{sh}^{3/2}} \\ R_{re,V_2} &= \frac{W_2 n_{re,V_2}^{3/2}}{n_{re,V_2}^{3/2} + n_{sh}^{3/2}}\end{aligned} \tag{C12}$$

For V_3, following the same assumptions as in V_1 and V_2, the relationship between R_{w,V_3} and R_{re,V_3} is derived as:

$$\frac{R_{b,V_3}}{R_{re,V_3}} = \frac{n_b^{3/2}}{n_{re,V_3}^{3/2}} \tag{C13}$$

The comprehensive hydraulic radius R_{V_3} within V_3 is derived as:

$$R_{V_3} = \frac{A_w + A_{re}}{\chi_w + \chi_{re}} = \frac{1 + n_w^{3/2}/n_{re,V_3}^{3/2}}{2} R_{re,V_3} \tag{C14}$$

The comprehensive hydraulic radius R_{V_3} is equal to half the width of the flow cross-section, that is, $R_{V_3} = W_3/2$. Thus, R_{re,V_3} is expressed as

Table D1
Error Statistics of the Depth-Averaged Maximum Longitudinal Velocity

Case	A1	A2	A3	A4	A5	B1	B2	B3	B4	B5
$u_{\max}$ (m/s)	0.325	0.339	0.404	0.396	0.510	0.360	0.384	0.461	0.433	0.585
$\varepsilon_{a,\max}$ (m/s)	0.003	0.0001	0.0003	0.0003	0.0013	0.00592	0.0003	0.0029	0.0017	0.00092
$\varepsilon_{r,\max}$ (%)	0.90	0.036	0.067	0.074	0.26	1.62	0.077	0.64	0.39	0.16
u_{sim} (m/s)	0.323	0.327	0.365	0.325	0.399	0.340	0.351	0.398	0.355	0.442
$\varepsilon_{a,\text{sim}}$ (m/s)	0.0055	0.012	0.039	0.071	0.11	0.027	0.034	0.066	0.079	0.14
$\varepsilon_{r,\text{sim}}$ (%)	1.72	3.65	10.64	21.94	27.94	7.86	9.62	16.50	22.24	32.42

$$R_{re,V_3} = \frac{W_3 n_{re,V_3}^{3/2}}{n_w^{3/2} + n_{re,V_3}^{3/2}} \tag{C15}$$

The expressions for the friction coefficients are obtained by substituting Equation C12 into Equation C4 and C6, and Equation C15 into Equation C6, yielding:

$$\begin{aligned} f_w &= \frac{8gn_w^2}{\left(\frac{W_1 n_b^{3/2}}{n_w^{3/2} + n_{sh}^{3/2}}\right)^{1/3}} \\ f_{re,V_2} &= \frac{8gn_{re,V_2}^2}{\left(\frac{W_2 n_b^{3/2}}{n_{re,V_2}^{3/2} + n_{sh}^{3/2}}\right)^{1/3}} \\ f_{re,V_3} &= \frac{8gn_{re,V_3}^2}{\left(\frac{W_3 n_{re,V_3}^{3/2}}{n_w^{3/2} + n_{re,V_3}^{3/2}}\right)^{1/3}} \end{aligned} \tag{C16}$$

Appendix D

This appendix section discusses the calculation of the depth-averaged maximum longitudinal velocity using the mass conservation method. The expressions for the depth-averaged maximum longitudinal velocity in each control volume are given below:

$$u_{\text{sim},V_1} = \frac{Q_m}{W_1 h} \tag{D1}$$

$$u_{\text{sim},V_2} = \frac{Q_t}{W_2 h} \tag{D2}$$

$$u_{\text{sim},V_3} = \frac{Q_m + Q_t}{W_3 h} \tag{D3}$$

where u_{sim,V_i} represents the depth-averaged maximum longitudinal velocity in each control volume calculated by the simplified method; W_i denotes the effective flow area in each control volume, which is determined using the same approach as in this study (Equation 12 and Equation B5). Table D1 systematically compares the simplified method, the calculation method proposed in this paper, and numerical prediction results, along with the relative errors between both calculated results and the true values.

As evidenced by the comparative results in Table D1, the calculation method proposed in this study demonstrates superior performance to the simplified approach. This enhancement stems primarily from the simplified method's neglect of shear stresses induced by recirculation zones, shear layers, and channel boundaries.

Conflict of Interest

The authors declare no conflicts of interest relevant to this study.

Data Availability Statement

The software version used in this paper is OpenFOAM-10, which is available for download at the link: https://openfoam.org/download/10-linux/ (Greenshields, 2022). All the data used in this study are available through DOI: 10.5281/zenodo.17721475 (Feng, 2025).

Nomenclature

η	Discharge ratio (−)
Q	Discharge (m^3/s)
W	Effective flow section (m)
W_d	Main channel width (m)
h	Water depth (m)
W_1, W_2, W_3	Width of control volume V_1, V_2, V_3 (m)
θ	Angle between the main and tributary channels (°)
θ'	Flow junction angle at the TDS (°)
S_0	Channel bed slope (−)
ρ	Fluid density (kg/m^3)
g	Gravitational acceleration (m/s^2)
τ	Shear stress (N/m^2)
u_{max}	Depth-averaged maximum temporal average velocity components in x directions (m/s)
$u_{max,re}$	Depth-averaged maximum velocity at the cross-section MCS (m/s)
u, v, w	Temporal average velocities in streamwise, lateral, and vertical directions (m/s)
$\overline{\varepsilon}_{xy}$	Depth-averaged eddy viscosity (m^2/s)
K	Secondary flow coefficient (−)
μ	Maximum flow contraction coefficient (−)
A	Effective cross-sectional area (m^2)
α	Energy correction coefficient (−)
β	Momentum correction coefficient (−)
P^*	Average hydrodynamic pressure exerted on the side walls of the tributary channel (N)
φ, ζ	Empirical coefficients in Equation 12 and Equation B4 (−)
f	Friction coefficient (−)
τ	Shear stress (N/m^2)
n	Manning roughness coefficient (−)
R	Hydraulic radius (m)
J	Hydraulic slope (−)
$\overline{\tau}$	Depth-averaged shear stress (N/m^2)
λ_d	Dimensionless comprehensive eddy viscosity (−)
y'	Position of depth-averaged maximum longitudinal velocity (m)
χ	Dimensionless wetted perimeter per unit width (−)
C_1, C_2, C_3	Integration constants in Equation 24 (−)

The following subscripts are used in this paper:

t, m	Abbreviations of the tributary and main channel
V_1, V_2, V_3	Abbreviations of control volume
re, sh, b, i	Abbreviations of the recirculation zone, interface, bed, and ice-cover shear stress layer

The following abbreviations are used in this paper:

MCS	Main channel maximum contracted section

TDS	Tributary downstream section
TUS	Tributary upstream section
MUS	Main channel upstream section.

Acknowledgments
This work was supported by the [Natural Science Foundation of Henan] (Grant [252300421946]), the [Open Research Fund of MWR Key Laboratory of Lower Yellow River Channel and Estuary Regulation] (Grant [LYRCER202202]), the [Yellow River Laboratory (Zhengzhou University) first-class project special fund project] (Grant [YRL221R11]), the [Scientific Research Projects of Power China Railway Construction Investment Group Co. Ltd] (Grant [DJ-ZSLJ-2023-01]), the [Significant Science and Technology Project of Ministry of Water Resources] (Grant [SKS-2022011]), and Yunnan Key Laboratory of Water Security (Grant 20254916CE340051).

References

Ashmore, P., Ferguson, R., Prestegaard, K., Ashworth, P., & Paola, C. (1992). Secondary flow in anabranch confluences of a braided, gravel-bed stream. *Earth Surface Processes and Landforms*, *17*(3), 299–311. https://doi.org/10.1002/esp.3290170308

Ashmore, P. E. (1982). Laboratory modelling of gravel braided stream morphology. *Earth Surface Processes and Landforms*, *7*(3), 201–225. https://doi.org/10.1002/esp.3290070301

Bahmanpouri, F., Barbetta, S., Gualtieri, C., Ianniruberto, M., Filizola, N., Termini, D., & Moramarco, T. (2022). Prediction of river discharges at confluences based on Entropy theory and surface-velocity measurements. *Journal of Hydrology*, *606*, 127404. https://doi.org/10.1016/j.jhydrol.2021.127404

Behzad, E., Mohammadian, A., & Yu, R. Q. (2024). Numerical simulation of confluence flow in a degraded bed. *Water*, *16*(1), 27. https://doi.org/10.3390/w16010085

Bennett, N. D., Croke, B. F., Guariso, G., Guillaume, J. H., Hamilton, S. H., Jakeman, A. J., et al. (2013). Characterising performance of environmental models. *Environmental Modelling & Software*, *40*, 1–20. https://doi.org/10.1016/j.envsoft.2012.09.011

Best, J. L. (1987). Flow dynamics at river channel confluences: Implications for sediment transport and bed morphology. *Recent Dev. Fluv. Sedimentol.*, 27–35. https://doi.org/10.2110/pec.87.39.0027

Biron, P. M., Buffin-Bélanger, T., & Martel, N. (2019). Three-dimensional turbulent structures at a medium-sized confluence with and without an ice cover. *Earth Surface Processes and Landforms*, *44*(15), 3042–3056. https://doi.org/10.1002/esp.4718

Boyer, C., Roy, A. G., & Best, J. L. (2006). Dynamics of a river channel confluence with discordant beds: Flow turbulence, bed load sediment transport, and bed morphology. *J. Geophys. Res.Earth Surface*, *111*(F4), F04007. https://doi.org/10.1029/2005JF000458

Bradbrook, K., Biron, P., Lane, S., Richards, K., & Roy, A. (1998). Investigation of controls on secondary circulation in a simple confluence geometry using a three-dimensional numerical model. *Hydrological Processes*, *12*(8), 1371–1396. https://doi.org/10.1002/(SICI)1099-1085(19980630)12:8<1371::AID-HYP620>3.0.CO;2-C

Bradbrook, K., Lane, S., & Richards, K. (2000). Numerical simulation of three-dimensional, time-averaged flow structure at river channel confluences. *Water Resources Research*, *36*(9), 2731–2746. https://doi.org/10.1029/2000WR900011

Celik, I. B., Ghia, U., Roache, P. J., & Freitas, C. J. (2008). Procedure for estimation and reporting of uncertainty due to discretization in CFD applications. *Journal of Fluids Engineering – Transactions of the ASME*, *130*(7), 078001. https://doi.org/10.1115/1.2960953

Chen, X., Zhu, D. Z., & Steffler, P. M. (2017). Secondary currents induced mixing at channel confluences. *Canadian Journal of Civil Engineering*, *44*(12), 1071–1083. https://doi.org/10.1139/cjce-2016-0228

Cheng, Z., & Constantinescu, G. (2018). Stratification effects on flow hydrodynamics and mixing at a confluence with a highly discordant bed and a relatively low velocity ratio. *Water Resources Research*, *54*(7), 4537–4562. https://doi.org/10.1029/2017WR022292

Constantinescu, G., & Gualtieri, C. (2024). River confluences: A review of recent field and numerical studies. *Environmental Fluid Mechanics*, *24*(6), 1143–1191. https://doi.org/10.1007/s10652-024-10002-4

Constantinescu, G., Miyawaki, S., Rhoads, B., & Sukhodolov, A. (2014). Numerical evaluation of the effects of planform geometry and inflow conditions on flow, turbulence structure, and bed shear velocity at a stream confluence with a concordant bed. *Journal of Geophysical Research - Earth Surface*, *119*(10), 2079–2097. https://doi.org/10.1002/2014JF003244

Constantinescu, G., Miyawaki, S., Rhoads, B., & Sukhodolov, A. (2016). Influence of planform geometry and momentum ratio on thermal mixing at a stream confluence with a concordant bed. *Environmental Fluid Mechanics*, *16*(4), 845–873. https://doi.org/10.1007/s10652-016-9457-0

Creelle, S., Schindfessel, L., & De Mulder, T. (2016). Modelling of the tributary momentum contribution to predict confluence head losses. *Journal of Hydraulic Research*, *55*(2), 175–189. https://doi.org/10.1080/00221686.2016.1212941

De Serres, B., Roy, A. G., Biron, P. M., & Best, J. L. (1999). Three-dimensional structure of flow at a confluence of river channels with discordant beds. *Geomorphology*, *26*(4), 313–335. https://doi.org/10.1016/S0169-555X(98)00064-6

Einstein, H. A. (1942). Formulas for the transportation of bed-load. *Trans. ASCE*, *107*(2140), 561–597. https://doi.org/10.1061/TACEAT.0005468

Ervine, D. A., Babaeyan-Koopaei, K., & Sellin, R. H. J. (2000). Two-dimensional solution for straight and meandering overbank flows. *Journal of Hydraulic Engineering - ASCE*, *126*(9), 653–669. https://doi.org/10.1061/(ASCE)0733-9429(2000)126:9(653)

Ettema, R. (2002). Review of alluvial-channel responses to river ice. *Journal of Cold Regions Engineering*, *16*(4), 191–217. https://doi.org/10.1061/(ASCE)0887-381X(2002)16:4(191)

Feng, H. (2025). Data of "A Semi-Analytical Model for Predicting the Maximum Depth-averaged Velocity in Fully Ice-Covered Confluence Channels" [Dataset]. *Zenodo*. https://doi.org/10.5281/zenodo.17721475

Fuentes-Pérez, J. F., Silva, A. T., Tuhtan, J., García-Vega, A., Baeza, R. C., Musall, M., & Kruusmaa, M. (2018). 3D modelling of non-uniform and turbulent flow in vertical slot fishways. *Environmental Modelling and Software*, *99*, 156–169. https://doi.org/10.1016/j.envsoft.2017.09.011

Greenshields, C. (2022). Openfoam user guide version 10 [Software]. The OpenFOAM Foundation, Ltd. Retrieved from https://openfoam.org/download/10-linux/

Gualtieri, C., Abdi, R., Ianniruberto, M., Filizola, N., & Endreny, T. (2020). A 3D analysis of spatial habitat metrics about the confluence of Negro and Solimoes Rivers Brazil. *Ecohydrology*, *13*(1), e2166. https://doi.org/10.1002/eco.2166

Guillén-Ludeña, S., Franca, M. J., Cardoso, A. H., & Schleiss, A. J. (2015). Hydro-morphodynamic evolution in a 90° movable bed discordant confluence with low discharge ratio. *Earth Surface Processes and Landforms*, *40*(14), 1927–1938. https://doi.org/10.1002/esp.3770

Guillén-Ludeña, S., Franca, M. J., Cardoso, A. H., & Schleiss, A. J. (2016). Evolution of the hydromorphodynamics of mountain river confluences for varying discharge ratios and junction angles. *Geomorphology*, *255*, 1–15. https://doi.org/10.1016/j.geomorph.2015.12.006

Hager, W. H. (1987). Separation zone at open-channel junctions – Discussion. *Journal of Hydraulic Engineering - ASCE*, *113*(4), 539–543. https://doi.org/10.1061/(ASCE)0733-9429(1987)113:4(539)

Hager, W. H. (1989). Transitional flow in channel junctions. *Journal of Hydraulic Engineering-ASCE*, *115*(2), 243–259. https://doi.org/10.1061/(ASCE)0733-9429(1989)115:2(243)

Holzner, J., Ostrander, T. S. P., Andreoli, A., Mazzorana, B., Comiti, F., & Gems, B. (2024). 2D numerical modeling of intense bedload-transport processes at confluences of mountain rivers and steep tributaries. *Natural Hazards*, *120*(3), 2255–2281. https://doi.org/10.1007/s11069-023-06212-6

Hsu, C. C., Wu, F. S., & Lee, W. J. (1998). Flow at 90° equal-width open-channel junction. *Journal of Hydraulic Engineering - ASCE*, *124*(2), 186–191. https://doi.org/10.1061/(ASCE)0733-9429(1998)124:2(186)

Jiang, C., Constantinescu, G., Yuan, S., & Tang, H. (2023). Flow hydrodynamics, density contrast effects and mixing at the confluence between the Yangtze River and the Poyang Lake channel. *Environmental Fluid Mechanics*, *23*(2), 229–257. https://doi.org/10.1007/s10652-022-09848-3

Jin, T., Ramos, P. X., Mignot, E., Riviere, N., & De Mulder, T. (2023). On the delineation of the flow separation zone in open-channel confluences. *Advances in Water Resources*, *180*, 104525. https://doi.org/10.1016/j.advwatres.2023.104525

Kakavandi, H., Heidari, M. M., & Ghobadian, R. (2024). A numerical model for calculating velocity distribution in cross-section of an open channel. *Applied Water Science*, *14*(3), 11. https://doi.org/10.1007/s13201-023-02090-2

Lau, Y. L., & Krishnappan, B. G. (1981). Ice cover effects on stream flows and mixing. *Journal of the Hydraulics Division*, *107*(10), 1225–1242. https://doi.org/10.1061/JYCEAJ.0005744

Lazzarin, T., Xu, L., Yuan, S., Hoitink, A. J. F., & Viero, D. P. (2026). Accounting for density driven secondary flows at river confluences with a 2-D depth-averaged hydro-morphodynamic model. *Environmental Modelling and Software*, *195*, 106735. https://doi.org/10.1016/j.envsoft.2025.106735

Leite Ribeiro, M., Blanckaert, K., Roy, A., & Schleiss, A. J. (2012a). Flow and sediment dynamics in channel confluences. *Journal of Geophysical Research*, *117*(F1), F01035. https://doi.org/10.1029/2011JF002171

Leite Ribeiro, M., Blanckaert, K., Roy, A., & Schleiss, A. J. (2012b). Hydromorphological implications of local tributary widening for river rehabilitation. *Water Resources Research*, *48*(10), W10528. https://doi.org/10.1029/2011WR011296

Lewis, Q., Rhoads, B., Sukhodolov, A., & Constantinescu, G. (2020). Advective lateral transport of streamwise momentum governs mixing at small river confluences. *Water Resources Research*, *56*(9), e2019WR026817. https://doi.org/10.1029/2019WR026817

Li, H., Sun, B., Li, Z. W., Li, D., Yang, Y. P., & Wang, F. F. (2024). Stage-discharge prediction in the multi-stage ice-covered compound channel. *Physics of Fluids*, *36*(6), 066607. https://doi.org/10.1063/5.0212575

Li, K., Yu, Q., Ma, X., Wang, L., & Nie, R. (2025). An improved physical model for open channel confluences: Bridging the gap between laboratory and field observations. *Water Resources Research*, *61*, e2025WR040229. https://doi.org/10.1029/2025WR040229

Liao, J. C., Beal, D. N., Lauder, G. V., & Triantafyllou, M. S. (2003). Fish exploiting vortices decrease muscle activity. *Science*, *302*(5650), 1566–1569. https://doi.org/10.1126/science.1088295

Liu, X. D., Li, L., Gu, L., Hua, Z., Zhang, Y., & Xue, H. (2021). Distribution and release of perfluorinated compounds (PFCs) in water-sediment systems: The effect of confluence channels. *Science of Total Environment*, *775*, 9. https://doi.org/10.1016/j.scitotenv.2021.145720

Luo, H., Fytanidis, D. K., Schmidt, A. R., & García, M. H. (2018). Comparative 1D and 3D numerical investigation of open-channel junction flows and energy losses. *Advances in Water Resources*, *117*, 120–139. https://doi.org/10.1016/j.advwatres.2018.05.012

Mahmodinia, S., & Javan, M. (2021). Vortical structures, entrainment and mixing process in the lateral discharge of the gravity current. *Environmental Fluid Mechanics*, *21*(5), 1035–1067. https://doi.org/10.1007/s10652-021-09808-3

Marzouk, O. A., & Huckaby, E. D. (2009). Effects of turbulence modeling and parcel approach on dispersed two-phase swirling flow. In *Proceedings of the World Congress on engineering and computer science 2009* (Vol. II). WCECS.

Morse, B., & Hicks, F. (2005). Advances in river ice hydrology 1999-2003. *Hydrological Processes*, *19*(1), 247–263. https://doi.org/10.1002/hyp.5768

Peters, M., Dow, K., Clark, S. P., Malenchak, J., & Danielson, D. (2017). Experimental investigation of the flow characteristics beneath partial ice covers. *Cold Regions Science and Technology*, *142*, 69–78. https://doi.org/10.1016/j.coldregions.2017.07.007

Prechtel, A. R., Coulter, A. A., Etchison, L., Jackson, P. R., & Goforth, R. R. (2018). Range estimates and habitat use of invasive Silver Carp (Hypophthalmichthys molitrix): Evidence of sedentary and mobile individuals. *Hydrobiologia*, *805*(1), 203–218. https://doi.org/10.1007/s10750-017-3296-y

Qiu, J., Yuan, S., Tang, H., Deng, Y., & Gualtieri, C. (2025). Hydrodynamic responses of fish community dynamics in large-scale morphologically complex river systems. *Water Resources Research*, *61*(7), e2025WR040690. https://doi.org/10.1029/2025WR040690

Rhoads, B., & Sukhodolov, A. (2001). Field investigation of three-dimensional flow structure at stream confluences: 2. Turbulence. *Water Resources Research*, *37*(9), 2411–2424. https://doi.org/10.1029/2001WR000317

Rhoads, B. L., & Johnson, K. K. (2018). Three-dimensional flow structure, morphodynamics, suspended sediment, and thermal mixing at an asymmetrical river confluence of a straight tributary and curving main channel. *Geomorphology*, *323*, 51–69. https://doi.org/10.1016/j.geomorph.2018.09.009

Rhoads, B. L., Riley, J. D., & Mayer, D. R. (2009). Response of bed morphology and bed material texture to hydrological conditions at an asymmetrical stream confluence. *Geomorphology*, *109*(3–4), 161–173. https://doi.org/10.1016/j.geomorph.2009.02.029

Rhoads, B. L., & Sukhodolov, A. N. (2004). Spatial and temporal structure of shear layer turbulence at a stream confluence. *Water Resources Research*, *40*(6), 13. https://doi.org/10.1029/2003WR002811

Rhoads, B. L., & Sukhodolov, A. N. (2008). Lateral momentum flux and the spatial evolution of flow within a confluence mixing interface. *Water Resources Research*, *44*(8), W08440. https://doi.org/10.1029/2007WR006634

Rice, S. P., Ferguson, R. I., & Hoey, T. B. (2006). Tributary control of physical heterogeneity and biological diversity at river confluences. *Canadian Journal of Fisheries and Aquatic Sciences*, *63*(11), 2553–2566. https://doi.org/10.1139/f06-145

Robert, A., & Tran, T. (2012). Mean and turbulent flow fields in a simulated ice-covered channel with a gravel bed: Some laboratory observations. *Earth Surface Processes and Landforms*, *37*(9), 951–956. https://doi.org/10.1002/esp.3211

Sandilya, S. S., Das, B. S., Devi, K., Khuntia, J. R., & Mohanty, M. P. (2025). CFD simulation of confluence of flow using different turbulence models. In *International conference on hydraulics, water resources and coastal engineering*. Springer. https://doi.org/10.1007/978-981-97-8035-8_14

Schindfessel, L., Creëlle, S., & De Mulder, T. (2015). Flow modes in an open channel confluence with increasingly dominant tributary inflow. *Water*, *7*(9), 4724–4751. https://doi.org/10.3390/w7094724

Schindfessel, L., Creëlle, S., & De Mulder, T. (2017). How different cross-sectional shapes influence the separation Zone of an open-channel confluence. *Journal of Hydraulic Engineering-ASCE*, *143*(9), 12. https://doi.org/10.1061/(ASCE)HY.1943-7900.0001336

Shaheed, R., Mohammadian, A., & Kheirkhah Gildeh, H. (2019). A comparison of standard k–ε and realizable k–ε turbulence models in curved and confluent channels. *Environmental Fluid Mechanics*, *19*(2), 543–568. https://doi.org/10.1007/s10652-018-9637-1

Shakibainia, A., Tabatabai, M. R. M., & Zarrati, A. R. (2010). Three-dimensional numerical study of flow structure in channel confluences. *Canadian Journal of Civil Engineering*, *37*(5), 772–781. https://doi.org/10.1139/L10-016

Shen, X., Gao, W. X., Cao, L. W., Li, S., Cai, H. J., Li, R., & Hodges, B. R. (2023). Characteristics of water free-surface with different momentum ratio at 45° confluence. *Journal of Hydrology*, *623*, 129787. https://doi.org/10.1016/j.jhydrol.2023.129787

Shen, X., Hodges, B. R., Li, R., Li, Z., Fan, J. L., Cui, N. B., & Cai, H. J. (2021). Factors influencing distribution characteristics of total dissolved gas supersaturation at confluences. *Water Resources Research*, *57*(6), 25. https://doi.org/10.1029/2020WR028760

Shen, X., Li, R., Cai, H., Feng, J., & Wan, H. (2022). Characteristics of secondary flow and separation zone with different junction angle and flow ratio at river confluences. *Journal of Hydrology*, *614*, 128537. https://doi.org/10.1016/j.jhydrol.2022.128537

Shen, X., Li, R., Hodges, B. R., Feng, J. J., Cai, H. J., & Ma, X. Y. (2019). Experiment and simulation of supersaturated total dissolved gas dissipation: Focus on the effect of confluence types. *Water Research*, *155*, 320–332. https://doi.org/10.1016/j.watres.2019.02.056

Shi, X., Jin, Q., Chen, H., Tao, H., & Song, T. (2025). Analysis of pollutant diffusion characteristics with intersection angle of 45° in environmental open channel. *International journal of Environmental Science and Technology*, *22*(7), 5543–5554. https://doi.org/10.1007/s13762-024-05953-6

Shiono, K., & Knight, D. W. (1991). Turbulent open-channel flows with variable depth across the channel. *Journal of Fluid Mechanics*, *222*, 617–646. https://doi.org/10.1017/S0022112091001246

Sui, J. Y., Wang, J., He, Y., & Krol, F. (2010). Velocity profiles and incipient motion of frazil particles under ice cover. *International Journal of Sediment Research*, *25*(1), 39–51. https://doi.org/10.1016/S1001-6279(10)60026-1

Sukhodolov, A. N., & Rhoads, B. L. (2001). Field investigation of three-dimensional flow structure at stream confluences: 2. Turbulence. *Water Resources Research*, *37*(9), 2411–2424. https://doi.org/10.1029/2001WR000317

Sukhodolov, A. N., Shumilova, O. O., Constantinescu, G. S., Lewis, Q. W., & Rhoads, B. L. (2023). Mixing dynamics at river confluences governed by intermodal behaviour. *Nature Geoscience*, *16*(1), 89–93. https://doi.org/10.1038/s41561-022-01091-1

Szupiany, R., Amsler, M. L., Hernandez, J., Parsons, D. R., Best, J. L., Fornari, E., & Trento, A. (2012). Flow fields, bed shear stresses, and suspended bed sediment dynamics in bifurcations of a large river. *Water Resources Research*, *48*(11), W11515. https://doi.org/10.1029/2011WR011677

Tang, H., Zhang, H., & Yuan, S. (2018). Hydrodynamics and contaminant transport on a degraded bed at a 90-degree channel confluence. *Environmental Fluid Mechanics*, *18*(2), 443–463. https://doi.org/10.1007/s10652-017-9562-8

Tsai, W., & Ettema, R. (1994). Modified eddy viscosity model in fully developed asymmetric channel flows. *Journal of Engineering Mechanics*, *120*(4), 720–732. https://doi.org/10.1061/(ASCE)0733-9399(1994)120:4(720)

Umar, M., Rhoads, B. L., & Greenberg, J. A. (2018). Use of multispectral satellite remote sensing to assess mixing of suspended sediment downstream of large river confluences. *Journal of Hydrology*, *556*, 325–338. https://doi.org/10.1016/j.jhydrol.2017.11.026

Wang, F., Huai, W., Guo, Y., & Liu, M. (2021). Turbulence structure and momentum exchange in compound channel flows with shore ice covered on the floodplains. *Water Resources Research*, *57*(4), e2020WR028621. https://doi.org/10.1029/2020WR028621

Wang, F., Huai, W., Liu, M., & Fu, X. (2020). Modeling depth-averaged streamwise velocity in straight trapezoidal compound channels with ice cover. *Journal of Hydrology*, *585*, 124336. https://doi.org/10.1016/j.jhydrol.2019.124336

Weber, L. J., Schumate, E. D., & Mawer, N. (2001). Experiments on flow at a 90 open-channel junction. *Journal of Hydraulic Engineering - ASCE*, *127*(5), 340–350. https://doi.org/10.1061/(ASCE)0733-9429(2001)127:5(340)

Yakhot, V., & Orszag, S. A. (1986). Renormalization group analysis of turbulence. I. Basic theory. *Journal of Scientific Computing*, *1*(1), 3–51. https://doi.org/10.1007/BF0106145

Yan, X. F., Duan, H. F., Yang, Q. Y., Liu, T. H., Sun, Y., & Wang, X. K. (2022). Numerical assessments of bed morphological evolution in mountain river confluences under effects of hydro-morphological factors. *Hydrological Processes*, *36*(2), e14488. https://doi.org/10.1002/hyp.14488

Yang, Q., Wang, X., Lu, W., & Wang, X. (2009). Experimental study on characteristics of separation zone in confluence zones in rivers. *Journal of Hydrologic Engineering*, *14*(2), 166–171.

Yu, Q., Yuan, S., & Rennie, C. D. (2020). Experiments on the morphodynamics of open channel confluences: Implications for the accumulation of contaminated sediments. *Journal of Geophysical Research - Earth Surface*, *125*(9), e2019JF005438. https://doi.org/10.1029/2019JF005438

Yuan, S. Y., Lin, H., Tang, H. W., Qiu, J. J., Li, Z. P., Xu, D., et al. (2024). An optimized entropy-based model for estimating river confluence hydrodynamics: Accounting for the effects of velocity dip. *Journal of Hydrology*, *628*, 14. https://doi.org/10.1016/j.jhydrol.2023.130408

Yuan, S., Qiu, J., Tang, H., Xu, L., Xiao, Y., Liu, M., et al. (2023). Fish community traits near a large confluence: Implications for its nodal effects in the river ecosystem. *Journal of Hydrology*, *626*, 130335. https://doi.org/10.1016/j.jhydrol.2023.130335

Yuan, S., Tang, H., Xiao, Y., Qiu, X., & Xia, Y. (2018). Water flow and sediment transport at open-channel confluences: An experimental study. *Journal of Hydraulic Research*, *56*(3), 333–350. https://doi.org/10.1080/00221686.2017.1354932

Yuan, S., Yan, G., Tang, H., Xiao, Y., Rahimi, H., Aye, M. N., & Gualtieri, C. (2023). Effects of tributary floodplain on confluence hydrodynamics. *Journal of Hydraulic Research*, *61*(4), 552–572. https://doi.org/10.1080/00221686.2023.2231413

Yuan, S., Zhu, Y., Tang, H., Xu, L., Li, K., Xiao, Y., & Gualtieri, C. (2022). Planform evolution and hydrodynamics near the multi-channel confluence between the Yarlung Zangbo River and the delta of the Niyang River. *Geomorphology*, *402*, 108157. https://doi.org/10.1016/j.geomorph.2022.108157

Yuan, S. Y., Tang, H. W., Xiao, Y., Qiu, X. H., Zhang, H. M., & Yu, D. D. (2016). Turbulent flow structure at a 90-degree open channel confluence: Accounting for the distortion of the shear layer. *Journal of Hydro-environment Research*, *12*, 130–147. https://doi.org/10.1016/j.jher.2016.05.006

Yuan, S. Y., Xu, L., Tang, H. W., Xiao, Y., & Gualtieri, C. (2022). The dynamics of river confluences and their effects on the ecology of aquatic environment: A review. *Journal of Hydrodynamics*, *34*(1), 1–14. https://doi.org/10.1007/s42241-022-0001-z

Zare, S. G. A., Moore, S. A., Rennie, C. D., Seidou, O., Ahmari, H., & Malenchak, J. (2016). Estimation of composite hydraulic resistance in ice-covered alluvial streams. *Water Resources Research*, *52*(2), 1306–1327. https://doi.org/10.1002/2015WR018096

Zhang, J., Wang, W., Li, Z., Li, Q., Zhong, Y., Xia, Z., & Qiu, H. (2021). Analytical models of velocity, Reynolds stress and turbulence intensity in ice-covered channels. *Water*, *13*(8), 1107. https://doi.org/10.3390/w13081107

Zhang, T., Feng, M., & Chen, K. (2023). The quantitative response of pollutant spatial distribution and mixing dynamics to confluent conditions in an asymmetric open-channel confluence. *Journal of Hydrology*, *620*, 129479. https://doi.org/10.1016/j.jhydrol.2023.129479

Zhang, X., Yu, D., Wang, H., Wan, A., Chen, M., Tao, F., & Song, Z. (2015). Effects of fish community on occurrences of Yangtze finless porpoise in confluence of the Yangtze and Wanhe Rivers. *Environmental Science and Pollution Research*, *22*(12), 9524–9533. https://doi.org/10.1007/s11356-015-4102-x

Zheng, L., Xu, J., Tan, Z., Xu, G., Xu, L., & Wang, X. (2020). A thirty-year Landsat study reveals changes to a river-lake junction ecosystem after implementation of the three Gorges dam. *Journal of Hydrology*, *589*, 125185. https://doi.org/10.1016/j.jhydrol.2020.125185

Zhong, Y., Huai, W. X., & Chen, G. (2019). Analytical model for lateral depth-averaged velocity distributions in rectangular ice-covered channels. *Journal of Hydraulic Engineering - ASCE*, *145*(1), 04018080. https://doi.org/10.1061/(ASCE)HY.1943-7900.0001557

Zhong, Y., Huai, W. X., Wang, Y. F., & Chen, G. (2018). Estimation of longitudinal dispersion coefficient in ice-covered Rivers. *Journal of Hydraulic Engineering - ASCE*, *144*(6), 9. https://doi.org/10.1061/(ASCE)HY.1943-7900.0001475